HHS Public Access

Author manuscript

Mol Cell. Author manuscript; available in PMC 2024 December 07.

Published in final edited form as:

Mol Cell. 2023 December 07; 83(23): 4334–4351.e7. doi:10.1016/j.molcel.2023.10.025.

EGFR Promotes ALKBH5 Nuclear Retention to Attenuate N6-Methyladenosine and Protect Against Ferroptosis in Glioblastoma

Deguan Lv[1], **Cuiqing Zhong**[1], **Deobrat Dixit**[2], **Kailin Yang**[3], **Qiulian Wu**[1], **Bhaskar Godugu**[4], **Briana C. Prager**[5], **Guofeng Zhao**[6], **Xiuxing Wang**[7], **Qi Xie**[8], **Shideng Bao**[9], **Chuan He**[10], **Dieter Henrik Heiland**[11], **Michael G Rosenfeld**[6], **Jeremy N. Rich**[1,12,13,*]

[1.]UPMC Hillman Cancer Center and Department of Medicine, University of Pittsburgh, Pittsburgh, PA 15213, USA

[2.]Sanford Burnham Prebys Medical Discovery Institute, La Jolla, CA 92037, USA

[3.]Department of Radiation Oncology, Taussig Cancer Center, Cleveland Clinic, Cleveland, OH 44195, USA

[4.]Department of Chemistry, University of Pittsburgh, Pittsburgh, PA 15260, USA

[5.]Department of Neurosurgery, Massachusetts General Hospital, Boston, MA 02114, USA

[6.]Howard Hughes Medical Institute, Department and School of Medicine, University of California, San Diego, CA 92093, USA

[7.]School of Basic Medical Sciences, Nanjing Medical University, Nanjing, Jiangsu 211166, China

[8.]Institute of Basic Medical Sciences, Westlake Institute for Advanced Study, Westlake University, Hangzhou, Zhejiang 310024, China

[9.]Department of Cancer Biology, Lerner Research Institute, Cleveland Clinic, Cleveland, OH 44195, USA

[10.]Department of Chemistry and Institute for Biophysical Dynamics, University of Chicago, Chicago, IL 60637, USA

[11.]Department of Neurosurgery, Medical Center - University of Freiburg, Freiburg, Germany

[12.]Department of Neurology, University of Pittsburgh, Pittsburgh, PA 15213, USA

[13.]Lead Contact

[*]Correspondence: drjeremyrich@gmail.com.

AUTHOR CONTRIBUTIONS

Conception and design, D.L. and J.N.R.; development of methodology, D.L., C.Z., Q.W., and J.N.R.; Acquisition of data, D.L., C.Z., B.G., D.H.H., G.Z., B.C.P., and Q.W.; analysis and interpretation of data, D.L., K.Y., Q.X., X.W., C.H., S.B., M.G.R., and J.N.R.; writing, reviewing, and/or revision of the manuscript, D.L., D.D., C.Z., K.Y., and J.N.R.

DECLARATION OF INTERESTS

The authors declare no competing interests.

SUMMARY

Growth factor receptors rank among the most important oncogenic pathways, but pharmacologic inhibitors often demonstrate limited benefit as monotherapy. Here, we show that epidermal growth factor receptor (EGFR) signaling repressed N^6-methyladenosine (m^6A) levels in glioblastoma stem cells (GSCs), whereas genetic or pharmacologic EGFR targeting elevated m^6A levels. Activated EGFR induced SRC to phosphorylate the m^6A demethylase, AlkB Homolog 5 (ALKBH5), thereby inhibiting Chromosomal Maintenance 1 (CRM1)-mediated nuclear export of ALKBH5 to permit sustained mRNA m^6A demethylation in the nucleus. ALKBH5 critically regulated ferroptosis through m^6A modulation and YTHDF2-mediated decay of the Glutamate-Cysteine Ligase Modifier Subunit (GCLM). Pharmacologic targeting of ALKBH5 augmented anti-tumor efficacy of EGFR and GCLM inhibitors, supporting an EGFR-ALKBH5-GCLM oncogenic axis. Collectively, EGFR reprograms the epitranscriptomic landscape through nuclear retention of the ALKBH5 demethylase to protect against ferroptosis, offering therapeutic paradigms for treatment of lethal cancers.

Graphical Abstract

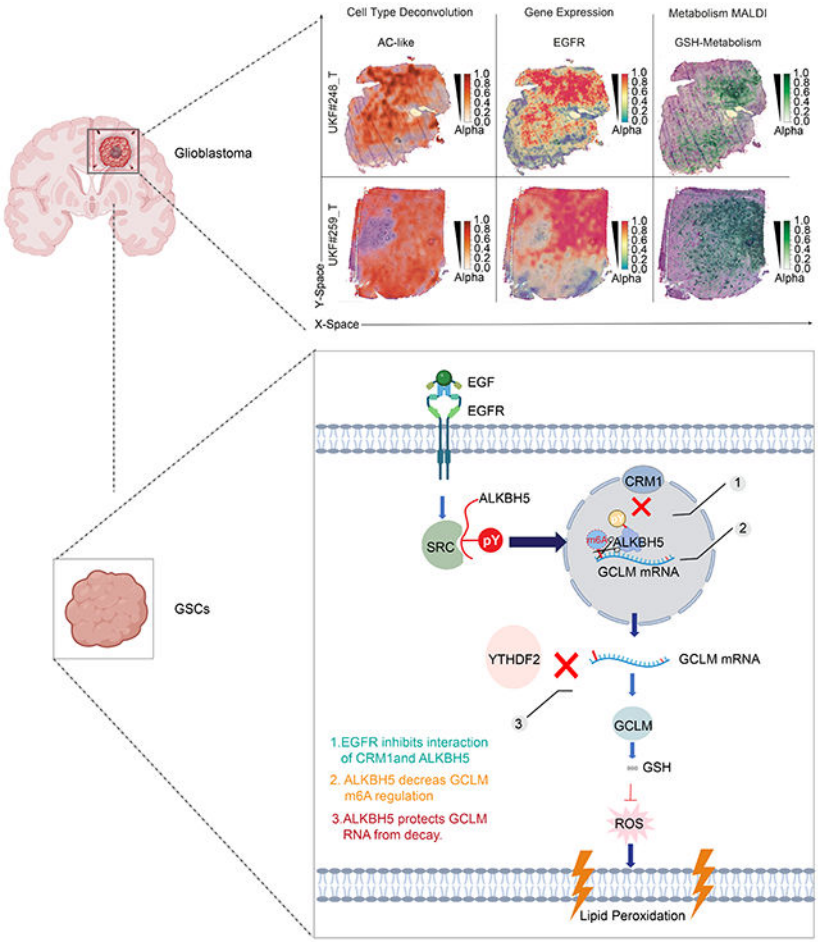

In brief

While growth receptor pathways commonly activate similar pathways, Lv et al show that EGF signaling represses m^{6}A levels in contrast to induction by PDGF. EGFR blocks ALKBH5 nuclear export, increasing m^{6}A eraser function and suppression of ferroptosis through glutathione production. ALKBH5 inhibitors enhance anti-tumor efficacy of EGFR or glutathione inhibitors.

Keywords

EGF; EGFR; SRC; ALKBH5; GCLM; YTHDF2; m^{6}A; glioblastoma; glioblastoma stem cell; cancer stem cell; ferroptosis; epitranscriptomics; growth factor receptor; tumor metabolism

INTRODUCTION

Glioblastoma, World Health Organization grade IV astrocytoma, is the most common primary intrinsic brain tumor. Recurrence after therapy is inevitable with median survival of glioblastoma patients limited to little more than a year.[1] Standard-of-care therapy includes maximal surgical resection followed by combined radiation and chemotherapy, and then adjuvant chemotherapy.[2] Treatment options for recurrent glioblastoma remain ineffective and largely palliative. Receptor tyrosine kinases (RTKs), including platelet-derived growth factor receptors (PDGFRs) and EGFR, are commonly dysregulated oncogenic pathways in glioblastoma, yet therapies targeting these pathways have repeatedly failed in glioblastoma clinical trials, suggesting the requirement of combinatorial targeting approaches for effective outcomes. EGFR and PDGFR have been linked to different transcriptional glioblastoma subtypes (classical and proneural, respectively),[3] yet both are frequently altered within tumors, demonstrating spatial intratumoral heterogeneity.[4] PDGFRβ is expressed by glioblastoma stem cells (GSCs) across transcriptional subtypes.[5] Vascular endothelial growth factor receptors (VEGFRs) are canonically expressed by endothelial cells, but GSCs also express VEGFRs, which promote their growth.[6] RTKs have been proposed to be interchangeable in activating intracellular pathways in glioblastoma,[7] supporting potential mechanisms of therapeutic failure, yet therapeutic paradigms targeting multiple RTKs have likewise failed in clinical trials for glioblastoma patients. Post-transcriptional RNA modifications, epitranscriptomics, are a level of glioblastoma regulation.[8-15] N^6-methyladenosine (m^{6}A) is regulated by a collection of writers and erasers, which are enzymes and amenable to therapeutic targeting, and readers, through which modifications become manifest.

Molecular epitranscriptomic regulators serve complex roles in cancer biology. The METTL3 methyltransferase has been reported as both an oncogene and tumor suppressor in glioblastoma.[10-13,16] Pharmacologic METTL3 inhibitors display anti-tumor efficacy.[17] The demethylases, which include fat mass- and obesity-associated protein (FTO) and ALKBH5, also contribute to tumor growth.[18,19] As both methyltransferases and demethylases promote glioblastoma growth, m^{6}A levels are not simply on-off switches, but rather contribute to the tumor growth based on the downstream targeted RNAs. PDGFR augments m^{6}A abundance in GSCs by transcriptional regulation of METTL3 to regulate mitophagy.[20] Here, we investigated the functions of EGFR signaling in GSCs. In contrast to the effects of PDGF, EGF signaling inhibited m^{6}A abundance in GSCs. EGF did not alter

the levels of m^{6}A writers or erasers but rather regulated the phosphorylation and nuclear localization of the m^{6}A demethylase ALKBH5. EGF regulation of ALKBH5 promoted resistance to a different metabolic process, ferroptosis, through the post-transcriptional regulation of GCLM, which is a rate-limiting step in glutathione production. Ferroptosis is biochemically distinct from general autophagy, apoptosis, and necrosis in that it involves an accumulation of cellular reactive oxygen species (ROS), an increase in free iron, and the disappearance of mitochondrial ridges.[21] GSCs display preferential uptake of iron, and targeting iron regulation leads to changes in FOXM1.[22] ALKBH5 likewise regulates FOXM1,[19] suggesting that ALKBH5 and ferroptosis may share molecular mechanisms. Thus, our study presents a link between EGFR signaling, m^{6}A modification, and ferroptosis opening avenues for combinatorial therapy for glioblastoma.

RESULTS

EGF signaling inhibits m^{6}A levels in glioblastoma

We recently reported that a gene expression signature generated from m^{6}A writers and erasers correlated with selected RTK pathways (notably PDGFR, VEGFR, and EGFR) in GSCs.[20] PDGFR increased m^{6}A levels through transcriptional induction of METTL3, whereas VEGF did not alter m^{6}A levels, suggesting that RTKs have distinct mechanisms in epitranscriptomics. EGFR and PDGFR are two important oncogenic genes in glioblastoma that have been linked to different transcriptional subtypes, yet both are frequently altered within tumors, demonstrating spatial intratumoral heterogeneity. Leveraging a recently reported spatial multiomics analysis of glioblastoma[23] provided tumor histology and cell type distribution (Figure 1A). Spatial GFR expression distribution in glioblastoma revealed that EGFR and PDGFRA were mutually exclusive (Figure 1B). EGFR correlated with radial glia niches and the astrocyte-like (AC-like) subtype, while PDGFR correlated with oligodendrocyte-progenitor-like (OPC) niches and neural-progenitor-like (NPC-like) subtype (Figures 1C, 1D, and S1A). Based on this background, we hypothesized that EGFR regulates m^{6}A levels through distinct mechanisms from PDGFR. EGFR stabilizes the m^{6}A reader, YTHDF2, in glioblastoma,[24] but YTHDF2 reduces tumor growth through destabilization of EGFR mRNA in hepatocellular carcinoma.[25] However, EGFR regulation of global m^{6}A levels remains unclear. We created a broad m^{6}A regulator signature to include writers (METTL3, METTL14, METTL16, VIRMA, RBM15, RBM15B, ZC3H13, and WTAP), erasers (FTO and ALKBH5), and readers/modulators (YTHDF1, YTHDF2, YTHDF3, YTHDC1, YTHDC2, HNRNPC, IGF2BP3, CBLL1, and HNRNPA2B1). The m^{6}A signature was associated with poor prognosis in glioblastoma patients from The Cancer Genome Atlas (TCGA) (Figure S1B). Glioblastomas were segregated into two clusters, which we designated as C1 (low) and C2 (high), based on the m^{6}A score (Figure S1C). Weighted correlation network analysis identified 10 co-expression modules in which the turquoise module positively correlated with selected tumor characteristics (Figure S1D) with enrichment of EGFR-related pathways (Figure S1E).

To directly investigate the role of EGFR in m^{6}A regulation, we interrogated a potential functional relationship in patient-derived GSCs. As GSCs are conventionally cultured with EGF, we removed EGF from the culture media for one week to avoid artifact, then

treated two patient-derived mesenchymal GSCs with a time course of EGF ligand to determine the effects of acute EGF ligand treatment on m^{6}A levels. Mesenchymal GSCs were selected because they are considered more aggressive.[26] EGF treatment progressively reduced m^{6}A levels measured using dot blots, colorimetric assays, and immunofluorescence (Figures 1E-G). As the anti-m^{6}A antibody is not entirely specific, we employed Liquid Chromatography–Mass Spectrometry (LC-MS) in parallel, which confirmed that EGF treatment decreased m^{6}A expression in GSCs (Figures 1H and 1I). In reciprocal loss-of-function studies, we treated GSCs with two clinically used EGFR inhibitors (erlotinib and lapatinib). Consistent with the gain-of-function studies, inhibiting EGFR increased m^{6}A levels (Figures S1F-S1K). EGFR can be activated in glioblastoma in the absence of ligand, including through the expression of a constitutively active variant EGFRvIII. EGFRvIII overexpression in GSCs reduced m^{6}A levels, suggesting that receptor activation phenocopies effects of EGF ligand (Figure S1L). To determine if EGF effects were disease-specific, we interrogated the effects of EGF on lung cancer cells, which are also frequently driven by EGFR signaling. In contrast to glioblastoma, EGF ligand did not appreciably decrease m^{6}A levels in lung cancer (Figure S1M). Collectively, these data demonstrate that, in contrast to the induction of m^{6}A by PDGFR, activated EGF signaling downregulates m^{6}A in GSCs.

EGF promotes ALKBH5 nuclear localization

To investigate the mechanism by which EGF signaling regulates m^{6}A, we measured the total protein expression of m^{6}A writers and erasers in GSCs after EGF treatment. EGF treatment did not alter the total protein levels of m^{6}A regulators in GSCs (Figure 2A). Likewise, treatment with EGFR inhibitors erlotinib and lapatinib had no effect on the protein levels of m^{6}A regulators (Figure 2B). As the intracellular distribution of the m^{6}A demethylase FTO determines the access of FTO to different RNA substrates,[27] we tested whether EGF altered the localization of m^{6}A regulators. EGF did not substantially alter the differential localization of FTO or the methyltransferase complex (METTL3, METTL14, and WTAP) in GSCs (Figures 2C and S2A). In contrast, EGF treatment induced the relocation of ALKBH5 from the cytoplasm into the nucleus (Figures 2C and 2D). In reciprocal loss-of-function studies, targeting EGFR expression in GSCs with shRNAs (Figure S2B) inhibited ALKBH5 nuclear localization (Figures 2E and 2F). In parallel pharmacologic studies, we treated GSCs with the EGFR inhibitor erlotinib, which increased cytoplasm ALKBH5 localization (Figure 2G). Expression of the constitutively active EGFR, EGFRvIII, promoted ALKBH5 nuclear localization in GSCs (Figure 2H). Other ErbB family members (ERBB2/3/4) do not directly bind EGF ligand but activate similar intracellular pathways and can form heterodimers with EGFR.[28] Knockdown the expression of each ErbB family member individually in GSCs did not appreciably alter ALKBH5 nuclear localization or m^{6}A global levels (Figures S2C-S2K). EGF treatment also did not significantly change ALKBH5 nuclear localization in lung cancers (Figure S2L), suggesting a disease-specific molecular regulation.

Next, we reasoned that EGF-induced ALKBH5 nuclear accumulation in GSCs could be due to increased nuclear import or decreased export into the cytoplasm. Therefore, we measured the effects of EGF treatment on ALKBH5 binding to importin (Importin α1: KPNA2, Importin β1: KPNB1) and exportin (CRM1). EGF treatment reduced the interaction between ALKBH5 and CRM1 (Figure S2M), which indicated that EGF inhibited ALKBH5 and

CRM1 binding to decrease ALKBH5 transport from nuclei into cytoplasm. Treatment with the CRM1 inhibitor, KPT330, rescued the erlotinib-induced ALKBH5 extranuclear transport and increased global m^6A levels (Figures S2N and S2O). Collectively, EGFR activity promotes reduced ALKBH5 export from the nucleus, where it functions to remove mRNA m^6A modifications.

EGF induces ALKBH5 phosphorylation to increase nuclear localization and m^6A demethylation

ERK phosphorylates METTL3 to regulate its function.[29] As protein phosphorylation can regulate the intracellular localization of numerous molecules, we next tested whether EGFR regulates m^6A levels and ALKBH5 intracellular localization through ALKBH5 phosphorylation. EGF treatment induced ALKBH5 tyrosine phosphorylation, but not serine or threonine phosphorylation, in GSCs (Figure 3A). In contrast, EGF treatment did not alter the phosphorylation of FTO or the methyltransferase complex in GSCs (Figures S3A-S3D). In parallel to effects of EGF ligand treatment, EGFR and EGFRvIII overexpression induced ALKBH5 phosphorylation (Figures 3B and 3C). Reciprocally, EGFR inhibitors decreased ALKBH5 phosphorylation in GSCs (Figure 3D).

Next, we explored if EGFR-mediated ALKBH5 phosphorylation was direct or indirect. Interactions between EGFR and ALKBH5 appeared weak (Figure S3E), whereas the intracellular signal transducer SRC strongly bound with ALKBH5 (Figure S3F). In contrast, other SRC family members did not bind to ALKBH5 (Figure S3F). The physical interaction between SRC and ALKBH5 mediated ALKBH5 phosphorylation, as targeting SRC genetically with shRNA or with a pharmacologic SRC inhibitor decreased the phosphorylation of ALKBH5 (Figures S3G and S3H). Further, SRC knockdown abolished the effects of EGF on ALKBH5 phosphorylation (Figure S3I). Expression of constitutively active mutant SRC in EGFR knockdown GSCs reversed ALKBH5 subcellular re-localization (Figures S3J and S3K). These results support SRC as a kinase responsible for ALKBH5 phosphorylation downstream of EGFR.

To define the specific amino acid residue(s) important for EGF-induced ALKBH5 phosphorylation, we predicted potential phosphorylation sites within ALKBH5 protein using GPS 5.0,[30] which suggested that a tyrosine at amino acid 71 was the highest likelihood site of phosphorylation by EGFR (Figure 3E) and SRC (Figure S3L). The tyrosine residue at position 71 is evolutionarily conserved in ALKBH5 homologs across species (Figure S3M). To assess the necessity of $ALKBH5^{Y71}$ (Figure S3N) for EGFR-induced ALKBH5 phosphorylation, we constructed shRNA-resistant ALKBH5 expression vectors with specific point mutations, Tyrosine 71 (Y71) to Phenylalanine (F71), or with another potential phosphorylation site, Tyrosine 306 (Y306) to Phenylalanine (F306) (Figure S3O). EGFR increased phosphorylation of wild-type $ALKBH5^{WT}$ and $ALKBH5^{Y306F}$, but not mutated $ALKBH5^{Y71F}$, in GSCs (Figure 3F). Next, we investigated the role of $ALKBH5^{Y71}$ on ALKBH5 intracellular localization and demethylase activity. GSCs were transduced with an shRNA to reduce endogenous ALKBH5 and then transduced with shRNA-resistant ALKBH5; EGF treatment promoted nuclear localization of $ALKBH5^{WT}$, but not $ALKBH5^{Y71F}$ (Figure 3G). As EGF inhibited ALKBH5 binding with nuclear

exportin CRM1 (Figure S2C), we tested whether ALKBH5 phosphorylation altered binding with CRM1. Consistent with the role of CRM1 binding in ALKBH5 localization, treatment with EGF inhibited binding of ALKBH5^{WT}, but not ALKBH5^{Y71F}, with CRM1 (Figure S3P). Thus, phosphorylation of ALKBH5 at Y71 is essential for ALKBH5 nuclear localization.

Next, we tested the effects of ALKBH5 phosphorylation on m^{6}A modification and tumor cell growth. GSCs with loss of ALKBH5 showed substantial levels of m^{6}A, which were markedly reduced with ALKBH5^{WT}, but not ALKBH5^{Y71F} (Figures 3H and 3I). The regulation of m^{6}A levels was reflected in tumor cell viability and in vivo tumor growth. Targeting ALKBH5 expression reduced both in vitro cell viability and in vivo tumor growth, which was fully rescued by re-expression of ALKBH5^{WT}, but not ALKBH5^{Y71F} (Figures 3J, 3K, and 3L). Together, our data demonstrate that EGF induces ALKBH5 Y71 phosphorylation, which is essential for ALKBH5 nuclear export and function in tumor cell viability and in vivo growth.

ALKBH5 regulates glutathione synthesis through GCLM

As ALKBH5 is essential for GSCs, we sought downstream mediators of its effects. Interrogating gene expression data from patient-derived GSCs, we found a set of genes that positively correlated with ALKBH5 expression, including RELB and TRIM39 (Figure S4A).[31] Among these genes, 796 genes were regulated by m^{6}A modification in GSCs (Figure S4B).[8] Classification of this group of genes revealed enrichment of NF-κB, MAP kinase pathway and ubiquitination, and protein modification (Figure S4C). To prioritize among these genes, we analyzed the expression of these genes in TCGA dataset: 196 genes were expressed at higher levels in glioblastoma surgical specimens compared with normal brain (Figure S4D). 68 genes were expressed at higher levels in GSCs compared with neural stem cells (NSCs) (Figure S4E). Venn diagramming revealed that a cluster of 17 genes with expression that correlated with ALKBH5, decorated with m^{6}A, and preferentially expressed in both GSCs and patient tumors (Figure 4A). Among these genes, we previously reported that GSCs display dependencies on JMJD6[32] and HEXB.[33] Among the remaining genes, FAM120A, SPATA6L, and CHST12 were not consistently correlated with patient survival in glioblastoma and all gliomas, whereas Glutamate-Cysteine Ligase Modifier Subunit (GCLM) correlated with poor survival (Figure S4F and S4G). GSCs expressed higher protein GCLM levels than NSCs (Figure 4B), astrocytes (Figure 4C), and differentiated glioblastoma cells (DGCs, Figure 4D). We explored whether this axis regulated the stemness of the GSCs. Targeting EGFR and ALKBH5 decreased stemness markers and increased differentiation marker expression in GSCs (Figures S4H and S4I), whereas targeting GCLM expression with shRNAs or activity with the inhibitor L-S, R-buthionine sulfoximine (L-S, R BSO) did not appreciably alter levels of GSC stemness markers or self-renewal (Figures S4J-S4M), suggesting that EGFR and ALKBH5, but not GCLM, regulate stemness.

Next, we considered the contributions of GCLM to glioblastoma viability and in vivo tumor growth. We transduced two patient-derived GSCs with either a control shRNA or one of two, non-overlapping shRNAs targeting GCLM. Loss of GCLM expression reduced tumor cell viability (Figure 4E) and survival of tumor-bearing mice (Figure 4F).

Based on the hypothesis that ALKBH5 regulated GCLM m^{6}A modification, we performed methylated (m^{6}A) RNA immunoprecipitation-quantitative polymerase chain reaction (MeRIP-qPCR), demonstrating that ALKBH5 knockdown increased GCLM methylation (Figure 4G). Supporting the role of ALKBH5 phosphorylation in downstream target regulation, the effects of ALKBH5 loss on GCLM m^{6}A modification were fully rescued by re-expression of ALKBH5^{WT}, but not ALKBH5^{Y71F} (Figure 4G), which indicates that the phosphorylation of ALKBH5 is essential for GCLM m^{6}A modification. We then tested the role of m^{6}A modification on GCLM expression. Targeting ALKBH5 in GSCs decreased GCLM protein levels measured by immunoblot and immunofluorescence, with the effects of ALKBH5 loss fully rescued by re-expression of ALKBH5^{WT}, but not ALKBH5^{Y71F} (Figures 4H and 4I). Confirming similar connections to EGFR signaling, treatment of GSCs with EGF ligand increased GCLM protein levels, whereas the EGFR pharmacologic inhibitor erlotinib reduced GCLM protein levels measured by immunoblot and immunofluorescence (Figures S4N-P). EGFR knockout decreased GCLM protein levels (Figure S4Q), whereas EGFRvIII expression increased GCLM protein levels measured by immunoblot (Figure S4R). As GCLM transcript levels correlated with ALKBH5 expression (Figure S4A), we explored how m^{6}A modification affected GCLM expression. ALKBH5 knockdown in two patient-derived GSCs decreased GCLM mRNA levels (Figure 4J). As m^{6}A modification often induces the decay of m^{6}A decorated mRNAs[34,35] and loss of ALKBH5 increased m^{6}A levels on GCLM, we hypothesized that GCLM transcript decay may be regulated by ALKBH5. Indeed, GSCs transduced with shALKBH5 displayed more rapid GCLM transcript decay (Figure 4K). YTHDF2 is an m^{6}A reader that can induce mRNA decay.[36-38] GSCs display higher levels of YTHDF2 than neural stem cells.[8] Therefore, we mapped YTHDF2 binding to GCLM transcripts using RBPsuite (Figure 4L).[39] To measure YTHDF2 binding to GCLM transcripts, we performed RNA immunoprecipitation followed by quantitative PCR (RIP-qPCR) using an IgG control or YTHDF2 antibody followed by qPCR for GCLM. Supporting the role of ALKBH5 in regulating YTHDF2 binding, shRNA targeting of ALKBH5 expression augmented YTHDF2 binding to GCLM mRNA (Figure 4M). Finally, we measured the effect of shALKBH5 on GCLM mRNA levels with and without a pharmacologic YTHDF2 inhibitor (DC-Y13-27), revealing that inhibiting YTHDF2 function restored GCLM levels altered upon ALKBH5 modulation (Figure 4N). Collectively, our data demonstrate that ALKBH5 increases GCLM mRNA levels by inhibiting YTHDF2-mediated decay.

GCLM is the rate-limiting step for glutathione (GSH) synthesis, so we measured GSH levels in GSCs with or without ALKBH5 knockdown. ALKBH5 knockdown decreased both total and reduced GSH levels, with the effects of ALKBH5 loss fully rescued by re-expression of ALKBH5^{WT}, but not ALKBH5^{Y71F} (Figure 4O). Supporting a role for GCLM as a downstream mediator for ALKBH5, GCLM expression rescued the effects of targeting ALKBH5 in vivo (Figure 4P and 4Q). Together, ALKBH5 regulates GCLM m^{6}A modification and protein levels to maintain tumor growth.

ALKBH5 promotes survival from ferroptosis by GCLM

Ferroptosis is an iron-dependent form of regulated cell death caused by unrestricted lipid peroxidation and subsequent membrane damage. Increased reactive oxygen species (ROS)

and lipid oxidization are two markers of ferroptosis.[21] Previous reports support a role for GSH in ferroptosis,[40] and a role of GCLM in regulation of ferroptosis in cancer.[41] GCLM knockdown induced GSC ferroptotic morphology and cell death (Figures 5A-C). Loss of GCLM also induced loss of immunofluorescence staining for Phen green SK (PGSK) diacetate, which is a fluorescent heavy metal indicator that reacts with a variety of metal ions, including Fe^{2+} (Figure S5A). Electron microscopy showed that GCLM knockdown in GSCs induced reduction in mitochondrial size, increased mitochondrial membrane density, and loss of mitochondrial ridges (Figure 5D). Targeting ALKBH5 expression phenocopied GSC structural alterations observed on electron microscopy and induction of cell death (Figures 5E and 5F). GCLM expression rescued the effects of targeting ALKBH5 on cell death (Figure S5B). To show that ALKBH5 induced ferroptosis through GSH regulation, we targeted ALKBH5 expression in GSCs, then measured the ability to rescue effects through providing reduced GSH. ALKBH5 knockdown decreased cell viability and increased SYTOX+ cell populations, which was completely reversed by the administration of reduced GSH (Figures 5G and 5H). Targeting ALKBH5 expression induced accumulation of ROS and oxidized lipids, which were reversed by the administration of reduced GSH (Figures 5I-L). To confirm ALKBH5 primarily induced cell death through ferroptosis, we blocked ferroptosis through treatment with iron chelators and synthetic lipophilic radical traps, which inhibited cell death and lipid peroxidation induced by a pharmacologic ALKBH5 inhibitor (Figures S5C and S5D). In contrast, induction of cell death by ALKBH5 inhibitor treatment was not rescued by treatment with caspase 3 inhibitors Z-DEVD-FMK and Ac-DEVD-CHO (Figure S5E), suggesting that apoptosis was not the primary mode of cell death. Likewise, ALKBH5 inhibitor treatment did not induce senescence (Figure S5F). Supporting a connection to GCLM, ferroptosis inhibitors blocked the induction of cell death and lipid peroxidation by GCLM inhibitor treatment (Figures S5G and S5H). To determine if EGF signaling regulates ferroptosis via GSH production, we measured GSC staining for PGSK upon erlotinib treatment or rescue with reduced GSH, revealing that GSH rescued the effects of erlotinib (Figure S5I). Genetic EGFR knockdown induced accumulation of ROS and lipid oxidation, which was rescued by GSH treatment (Figures S5J-S5L). Thus, EGFR-ALKBH5-GCLM protects against ferroptotic cell death through GSH regulation.

Pharmacologic targeting of ALKBH5 augments the antitumor efficacy of EGFR inhibition

Concordant with the regulation of ALKBH5 function and GCLM downstream of EGFR, both EGFR and GCLM were strongly associated with increased tumor grade and molecular features associated with poor patient outcome in TCGA (Figure S6A). Enrichment of ALKBH5 mRNA was lower, as expected by the post-translational regulation of ALKBH5. ALKBH5 functions as an enzymatic demethylase with recent reports describing small molecules that inhibit ALKBH5.[42] We selected an FDA-approved EGFR inhibitor (erlotinib) and two compounds that inhibit ALKBH5 enzymatic activity [designated as ALKBH5 inhibitor 1 (ALKBH5i1) and ALKBH5 inhibitor 2 (ALKBH5i2)] (Figure 6A). All three agents inhibited GSC proliferation as monotherapy with concentration dependence (Figure S6B). Treatment with ALKBH5 inhibitors increased m^6A levels in GSCs, supporting on-target effects of the ALKBH5 inhibitors (Figure 6B). To confirm that the molecular target of the putative ALKBH5 inhibitors was on-target, we leveraged the crystal structure of ALKBH5 with consideration of the key residues for enzymatic activity, N193 and H204[42]

to design a drug-resistant mutant ALKBH5 (ALKBH5$^{N193K/H204P}$) (Figure S6C). GSCs expressing WT ALKBH5 but not the mutant ALKBH5 were sensitive to the ALKBH5i (Figure S6D). Based on the molecular interactions between EGFR and ALKBH5, we hypothesized that combined treatment with these inhibitors could offer greater anti-tumor efficacy. ALKBH5 inhibitors augmented the efficacy of erlotinib against GSCs (Figure 6C).

To test potential combinatorial benefit between ALKBH5 and EGFR inhibitors in vivo, we treated mice bearing luciferase transduced GSCs with each small molecule compound as monotherapy or in combination (Figure S6E). Administration of either ALKBH5i or erlotinib had similar efficacy as a single agent reducing tumor growth *in vivo*, with combinatorial treatment showing greater reduction of tumor volume (Figures 6D and S6F). Reduced tumor growth translated into prolonged survival of orthotopic tumor-bearing mice with each agent as monotherapy and improved survival as combinations (Figures 6E-G). To be a viable brain tumor therapy, drugs need to have a therapeutic index and delivery into the central nervous system, so we assessed the toxicity and distribution of these drug combinations *in vivo*. Treatment with the EGFR and ALKBH5 inhibitors as either monotherapy or in combination did not induce laboratory signs of liver toxicity, as measured by serum levels of aspartate aminotransferase and alanine aminotransferase activity (Figures 6H and 6I), nor induced histologic indications of damage to the liver, kidney, or heart (Figure 6J). To measure drug delivery, we treated mice bearing glioblastoma orthotopic xenografts with EGFR or ALKBH5 inhibitors, then we collected serum, tumor, and non-tumor brain to measure drug levels. At the doses tested, each agent showed evidence of delivery into the non-tumor bearing brain and intracranial tumor (Figure S6G).

Next, we compared the survival of glioblastoma patients in both the TCGA and Chinese Glioma Genome Atlas (CGGA) based on expression of EGFR and ALKBH5. Patients whose tumors expressed high levels of both EGFR and ALKBH5 had a worse prognosis than those with lower expression (Figures 6K and 6L). Taken together, ALKBH5 represents a potential therapeutic target in combination with EGFR for patients afflicted with glioblastoma.

Pharmacologic targeting of ALKBH5 augments antitumor efficacy of a GCLM inhibitor

Agents that induce ferroptosis have been described as potential adjuvant anti-cancer treatments.[43] Cancer cells have higher iron metabolic demands, making them more susceptible than normal cells to ferroptosis[21], and GSCs preferentially traffic iron.[22] GSCs displayed relative resistance to ferroptosis inducers compared with DGCs (Figures S7A and S7B). Targeting GCLM had limited toxicity against NSCs and astrocytes suggesting that GCLM may be a preferential target against glioblastoma (Figures S7C and S7D). BSO is a potent specific and selective irreversible inhibitor of GCLM[44-48] (Figure 7A). BSO induced ferroptosis (Figure S7E) and displayed preferential activity against GSCs relative to DGCs (Figure 7B). Like EGFR and ALKBH5, ALKBH5 and GCLM appear to be linked sequentially, but most molecular nodes have multiple inputs and outputs, including feedback mechanisms. This has led to combinatorial approaches with vertically integrated therapeutics, notably BRAF and MEK inhibitors in melanoma.[49-51] We hypothesized that combinatorial targeting of ALKBH5 and GCLM could display additional benefit. Indeed,

in vitro combinations of inhibitors of ALKBH5 and GCLM displayed synergistic anti-GSC efficacy (Figures 7C and 7D). Mice bearing glioblastoma orthotopic xenografts transduced with a bioluminescence marker underwent treatment with vehicle control, ALKBH5 inhibitor, GCLM inhibitor, or the combination. Treatment with either ALKBH5i or GCLM inhibitor alone reduced *in vivo* tumor volume, with additional benefit of combined therapy in vivo (Figures 7E and S7F). Reduced tumor volumes translated into prolonged survival with combined therapeutic benefit with the ALKBH5 and GCLM inhibitors (Figures 7F-H). Measurement of GCLM inhibitor delivery into the brain and intracranial tumor relative to blood levels demonstrated modest but effective levels (Figure S7G).

Finally, we considered the prognostic significance of signatures with ALKBH5-GCLM, EGFR-GCLM, and EGFR-ALKBH5-GCLM. Consistent with the EGFR-ALKBH5-GCLM axis contributing to the malignancy of glioma, each signature displayed significance when tumors expressed high levels of the molecular target (Figures S7H and S7I). To confirm the connection between EGFR and GCLM in the absence of cell culture, we interrogated the spatial transcriptomics and metabolomics data from glioblastoma patient specimens. EGFR and GCLM mRNA correlated at the single cell level (Figure 7I), and EGFR mRNA levels spatially correlated with glutathione metabolism (Figures 7J and 7K), although not exclusively. Taken together, targeting epitranscriptomic regulation and ferroptosis in combination represents a potential therapeutic paradigm for glioblastoma (Figure S7J).

DISCUSSION

Approximately 0.1-0.4 percent of all the adenine bases in mammalian mRNAs are methylated by m^6A, making m^6A a highly dynamic and tightly regulated post-transcriptional modification that influences the dynamics of transcriptome.[52] Although discovered in 1970s,[53,54] the functions of m^6A modification in dynamic regulation of transcriptome have only recently been appreciated. In GSCs, METTL3 is regulated by the YY1 transcription factor and PDGF signaling.[9,20] Here, the identification of an EGF-ALKBH5-GCLM axis in GSCs presents a mechanism to evade ferroptosis-mediated cell death in glioblastoma.

EGFR signaling induces proliferation in numerous cell types, including cancer cells.[55] EGFR expression, amplification, and mutations have been associated with poor prognosis and chemoresistance in glioblastoma.[56] Numerous TKIs targeting EGFR have been examined in relation to glioblastoma. First-generation reversible small-molecule inhibitors, erlotinib and gefitinib, showed promising results in preclinical experiments, they remain largely ineffective in subsequent clinical trials.[57] m^6A modifications mediate gefitinib resistance in lung adenocarcinoma.[58] Here, we found a suppressive effect of EGFR on global mRNA m^6A levels via regulation of ALKBH5 nuclear localization. The nuclear localization of ALKBH5 was dependent on EGFR-mediated phosphorylation at a specific phosphorylated residue (Y71) on ALKBH5 mediated by SRC activated by EGFR. The substrate specificity and functions of m^6A modifying enzymes depend on their subcellular localization and their interactions with diverse interacting proteins,[59] but we are unaware of such studies for ALKBH5. The m^6A demethylase functions of ALKBH5 are largely nuclear and regulated by EGF-EGFR-SRC mediated phosphorylation of ALHBH5 on the Y71 reside

to inhibit its nuclear export by reducing ALKBH5 binding to nuclear exportin, CRM1, leading to ALKBH5 nuclear accumulation and promotion of its demethylase activity.

GCLM was a direct target of the EGFR-ALKBH5 axis in GSCs, as ALKBH5 depletion or loss of Y71 phosphorylation decreased GCLM levels in an m^6A-dependent manner. GCLM contributes to the first rate-limiting step in glutathione (GSH) synthesis, and antioxidant functions of GSH are critical for the initiation of various cancers. High GCLM levels are associated with poor prognosis of cancer patients.[60] Here, GCLM regulates ferroptosis in GSCs. ALKBH5 and GCLM depletion led to ferroptosis-mediated cell death. Modulating ferroptosis has anti-cancer effects in experimental preclinical cancer models, prompting the development of pharmacologic agents. Our study establishes a link between EGFR signaling, RNA m^6A modification, and ferroptosis, suggesting potential combinatorial therapy.

Glioblastoma modulates the downstream effectors of RTKs in response to microenvironmental factors and therapies, suggesting simultaneous targeting of multiple components of such signaling pathways will be essential to avoid drug resistance. Our results suggest that combined targeting of EGFR and ALKBH5 holds promise, with combinatorial benefits of erlotinib and a ALKBH5 inhibitor, both in vitro and in vivo. Sensitivity to ferroptosis depends on genes and pathways involved in ROS, iron, lipid, and energy metabolism. Although GSCs were resistant to conventional ferroptosis inhibitors, a GCLM inhibitor selectively inhibited GSC growth and tumor formation. GCLM and ALKBH5 inhibitors showed synergistic effect on GSC growth. These results suggest that targeting multiple nodes in this pathway may be beneficial, potentially suggesting the existence of positive feedback loops or multiple interactions that require disruption for optimal therapeutic efficacy. Collectively, these pharmacological combinations warrant further investigation.

LIMITATIONS OF THE STUDY

Several questions remain for future consideration. The differential downstream effects of EGFR and PDGFR signaling suggest that microenvironmental metabolic demands drive evolutionary selection of specific growth factor signaling in glioblastoma specifically. The synergistic effects of targeting multiple nodes with EGFR, ALKBH5, and GCLM highlight that there are likely multiple inputs and outputs to each node with potential feedback mechanisms that could inform improved therapeutic design. Like all precision medicine efforts, optimization of combined treatment paradigms will require selection of agents based on target inhibition; off-target effects; duration, sequencing, and timing of treatment; and delivery. Establishing a successful in vivo synergy will inform the translation of these therapeutic paradigms into future clinical trials.

STAR ★ METHODS

RESOURCE AVAILABILITY

Lead contact—Further information and requests for resources and reagents should be directed to and will be fulfilled by the lead contact, Jeremy Rich (drjeremyrich@gmail.com).

Materials availability—This study did not generate new unique reagents.

Data and code availability

- This paper analyzes existing, publicly available data from GSE158742 and GSE119834. These accession numbers for the datasets are listed in the key resources table.
- This paper does not report original code.
- Any additional information required to reanalyze the data reported in this paper is available from the lead contact upon request.

EXPERIMENTAL MODEL AND STUDY PARTICIPANT DETAILS

GSC derivation—All GSCs were derived from the primary patient tumors after review by a neuropathologist and used in accordance with an approved protocol by the Institutional Review Board at Cleveland Clinic. As previously described,[20] GSCs were derived immediately after dissociation of primary patient tumor. Freshly resected tumor tissues were enzymatically and mechanically dissociated into single cells and grown in the neurobasal medium supplemented with serum-free B-27 supplement (Invitrogen), 20 ng/mL EGF and 20 ng/mL FGF, sodium pyruvate, GlutaMAX, and 1000 U/mL Penicillin-Streptomycin supplement for 2-4 weeks. Free-floating neutrospheres were harvested and subsequently maintained in the previously mentioned neurosphere medium, with cell dissociation performed every 5–6 days as part of the routine culture. The 1919 GSC model was derived from a 53-year-old male patient with GBM. MES20 was provided as a generous gift by Dr. Erik Sulman which was derived from a female patient with GBM.[26] To minimize the incidence of cell culture-based artifacts, patient-derived xenografts were produced and propagated as a renewable source of tumor cells for this study. Short tandem repeat (STR) analyses were performed on the tumor cells for authentication on a yearly basis. Cells were frozen and stored in liquid nitrogen when not being actively cultured.

Cell culture—All cells were cultured in 5 % CO_2 incubator at 37 °C. Human HEK293T cells from American Type Culture Collection and astrocyte cells from ScienCell were cultured in DMEM with 10% fetal bovine serum. Neural stem cells (ENSA, HPN1, and NSC11) and GSCs were cultured in Neurobasal medium supplemented with serum-free B-27 supplement, 20 ng/mL EGF and 20 ng/mL FGF, sodium pyruvate, GlutaMAX, and 1000 U/mL Penicillin-Streptomycin supplement. Short tandem repeat analyses were performed to authenticate the identity of each tumor model used at least annually. Mycoplasma testing with qPCR was performed on supernatants from cell culture at least annually. Cells were stored in liquid nitrogen when not being actively cultured.

Plasmid Isolation and Site-Directed Mutagenesis—The shRNA or overexpressed plasmids were amplified by transformation (ThermoFisher). Bacteria were cultured in LB medium. Plasmids were then isolated using PureLink™ HiPure Plasmid Midiprep Kit (ThermoFisher). Plasmid concentrations were determined by absorbance test at 260 nm using the NanoDrop One device (Thermo Scientific). Site directed mutagenesis was performed on pcDNA3-ALKBH5 by using the

Q5® Site-Directed Mutagenesis (NEB) according to manufacturer's instructions. Mutations were verified via commercial Sanger sequencing (Eton). The primers for ALKBH5 Y71F construction were 5'- Gagcgcagcgactttgaggagcagcagctgc-3' and 5'- GCTCCTCAAAGTCGCTGCGCTCGGGGTCCGA-3', for ALKBH5 Y306F were 5'-AcccagctTtgcttcagatcgcctgtcagga-3' and 5'-GCGATCTGAAGCAAAGCTGGGTGGTAACACG-3', the primer for shRNA-resistant ALKBH5 were 5'-ccgtgttaccgccaagttatgcttcagatcgcct-3' and 5'-aagcataacttggcggtaacacggagctgctcag-3'.

Retroviral packaging and infection—To stably knock down (using shEGFR, shALKBH5, shGCLM, or shSRC) or overexpress (EGFR, ALKBH5, or GCLM) of selected molecular targets or relevant controls (shCONT or EV) in GSCs, we performed virus package and infection with the recombinant lentivirus. 6 μg transfer plasmid mix with 4 μg pxpax2, 2 μg plp/vsvg, and LipoD293 (SignaGen Laboratories) were co-transfected into HEK293T cells. Lentivirus was extracted from the supernatant collected in 48 and 72 hours after transfection with Lenti-X concentrator (Takara Bio) according to the manufacturer's protocol. Lentivirus and 10 μg / mL polybrene were used to transduce the GSCs for 24 hours. Infected cells were selected with 2μg / mL puromycin for 7 days. The efficiency of infection was detected by qPCR and Immunoblottingting.

In vivo tumorigenesis—All animal experiments were conducted in accordance with the guidelines of the Institutional Animal Care and Use Committee–approved protocol (IACUC) of the University of Pittsburgh. Healthy, wild-type male or female mice of NSG (NOD.Cg-Prkdcscid Il2rgtm1Wjl/SzJ; The Jackson Laboratory) background, 4 to 6 weeks old, with no prior treatment were randomly selected and used in this study for intracranial injection. Mice were housed 4-5 per cage unless otherwise stated. Intracranial xenografts were generated by implanting 20,000 patient derived GSCs into the right cerebral cortex of mice at a depth of 3.5 mm. Housing conditions and animal status were supervised by a veterinarian. Euthanasia was taken until neurologic symptoms included hunched posture, gait changes, or lethargy were observed, at which point they were sacrificed. Brains were harvested and frozen at −80 °C with O.C.T. compound (4583, Tissue-Tek) directly or fixed in 4 % formaldehyde for 48 hours then stored in 70 % ethanol, and sectioned. Hematoxylin and eosin staining was performed on sections for histologic analysis using H&E Staining Kit (Hematoxylin and Eosin) (ab245880, ABcam) based on the manufacturer's protocol.

Patient database and bioinformatics—The Kaplan-Meier survival analysis with the log-rank test was used to assess prognostic significance of every gene in the TCGA and CGGA GBMLGG RNA-seq datasets. The processed UCSC TOIL analysis of TCGA and GTEx RNA-seq data were used to determine genes that were differentially expressed between GBM specimens and normal brain specimens.[61] The Cox Proportional Hazards model and log-rank analysis were used to assess prognostic significance of each selected gene in the TCGA and CGGA dataset.

METHOD DETAILS

Cell viability—GSC viability assays were performed after target gene knockdown, overexpression, or drug treatment. The cells were incubated with basal medium overnight then seeded 1×104 cells in each well of a 96-well plate. The luminescence assay was performed using CellTiter-Glo according to the manufacturer's instructions (Promega). Briefly, 1 x 10^4 cells were seeded in one well of a 96-well plate. After treatment, equal amounts of medium of the mixture of reagents A and B were added to the 96-well plates and incubated for 15 minutes with gentle shaking. The luminescence was detected in a plate reader according to the manufacturer's instructions.

Cell fractionation—Cells were spined down at 350 x g for 5 min and were resuspended in 0.5 ml of cold 1X PBS. Aliquoting 100 µl of cell suspension into a 1.5 ml tube for the whole cell lysate (WCL). The remaining 400 µl cell suspension was centrifuged for 5 min at 500 x g at 4°C. Cell pellet was resuspended in 500 µl of CIB and incubated on ice for 5 min. Then, the lysate was centrifuged for 5 min at 500 x g. The suspension is the cytoplasmic fraction. 500 µl MIB was used to resuspend the pellet. Incubation on ice for 5 min. The membrane and organelle Fraction can be obtained after centrifuging for 5 min at 8,000 x g. The pellet was resuspended in 250 µl of CyNIB. The nuclear fraction was obtained for 5 sec sonication at 20% power.

Immunoblotting—Briefly, 1 x 10^6 cells were lysed in 200 µL RIPA lysate buffer with proteinase inhibitor (4693116001, Sigma) and phosphatase inhibitor (4906837001, Sigma) on ice after being treated under varying conditions as indicated. Protein lysates or cellular fraction were separated by SDS-PAGE gel then was transferred to PVDF membrane (IPVH00010, Millipore Sigma). The PVDF membrane was blocked with Blocker™ Casein in PBS (37582, ThermoFisher), then incubated with the primary antibody of p-EGFR (1:1000), EGFR (1:1000), Src (1:1000), GCLM (1:1000), VIRMA (1:1000), METTL3 (1:1000), ALKBH5 (1:1000), FTO (1:1000), METTL14 (1:1000), WTAP (1:1000), VIRMA (1:1000), LAMIN B1 (1:5000), p-S/T(1:1000), P-y (1:3000), KPNA2 (1:1000), KPNB1 (1:1000), CRM1 (1:1000), ERBB1 (1:1000), ERBB2 (1:1000), ERBB3 (1:1000), EGFRvIII (1:1000), Laminb1 (1:5000) or GAPDH (1:10000) for 2 hours at room temperature or 4 °C overnight. PVDF membranes were washed with TBST for 4 times of a total 1 hour and incubated with anti-rabbit lgG HRP-linked antibody (1:1000) or anti-mouse lgG HRP-linked antibody (1:1000) for another 2 hours. Images were captured by a BIO-RAD workstation and gray values were analyzed using image-analysis software AlphaImager 2200 (ProteinSimple, San Jose, CA, USA).

Immunofluorescence analysis—Cells were plated on 12-mm round glass coverslips coated with Matrigel (Corning) in a 24-well plate in a humidified chamber at 37 °C and 5 % CO_2 for 12 hours. For SYTOX and PGSK staining, cells were cultured with SYTOX and PGSK dye for 30 minutes. For immunofluorescence studies, cells were washed with chilled PBS (pH 7.2) twice and fixed in 4% paraformaldehyde for 20 minutes on ice and then permeabilized with 0.2% Triton X-100 for 10 minutes. After washing with cold PBS twice, cells were blocked with 5% goat serum for 30 minutes, then incubated overnight with selected antibodies: ALKBH5 (1:100), METTL3 (1:50), METTL14 (1:100), WTAP

(1:100), LAMINB1 (1:500), GCLM (1:100). Cells were incubated with Alexa Fluor 488 (568) goat anti-rabbit IgG or goat anti-mouse lgG for 2 hours. After washing, the cells were treated with a 1:1000 solution of DAPI in PBS for 5 minutes, washed and blocked with PVF medium. Images were acquired with Leica fluorescence microscope or LSM710 confocal microscope (40 x oil objective) and Nikon A1R (63 x oil objective).

Co-immunoprecipitation (IP)—The co-immunoprecipitation was performed as previous description.[62] In brief, cells were washed with chilled PBS after treatment under selected conditions. Protein was extracted with IP lysate (87787,ThermoFisher), pre-cleared with 30 μl protein G/A-plus agarose beads (sc-2003, Santa Cruz Biotechnology) for 1 hour at 4 °C and the supernatant was obtained after centrifugation (5,000 rpm) at 4 °C. Precleared homogenates (supernatants) were incubated with 2 μg of antibody and/or normal mouse/ rabbit IgG by rotation for 4 hours at 4 °C, then immunoprecipitates were incubated with 30 μl protein G/A-plus agarose beads by rotation overnight at 4 °C, and then centrifuged at 5000 rpm for 5 min at 4 °C. The precipitates were washed five times for 10 min with beads wash solution (50 mM (pH 7.6) TrisCl, 150 mM NaCl, 0.1% NP-40, 1 mM EDTA) and then resuspended in 60 μl 2× SDS-PAGE sample loading buffer to incubate for 10 min at 100°C. Immunoblotting was performed with pertinent antibody as indicated.

mRNA purification—PolyA-mRNA was purified using magnetic mRNA isolation kit (NEB) according to the manufacturer's instructions. Briefly, GSCs were pelleted by centrifuging at 1,000 rpm for 5 minutes at 4 °C, then pelleted again after washing with cold sterile 1X PBS (pH 7.4). 500 μL lysis buffer was added to the cells and incubated at RT for 5 minutes with gentle agitation. The lysates were moved to 100 μL beads and mixed at RT for 10 minutes. The lysates were removed, and the pellets were washed with 500 μL wash buffer for 1 minute twice. Beads were then washed with 500μL low salt buffer with agitation for 1 minute and the wash solution was discarded. 100 μL elution buffer was added and vortexed gently to suspend beads and incubate at 50°C for 2 minutes. Eluent which contains the PolyA-mRNAs was transferred to a clean tube.

m^{6}A dot blot—200 ng RNA from selected cells was denatured at 95 °C for 3 minutes then chilled on ice immediately for 2 minutes. The mRNA was then dropped directly onto Hybond-N+ membranes. Spotted mRNA was crosslinked to the Hybond-N+ membranes in a UV crosslinker twice using the following mode (1,200 microjoules [x100]; 25 seconds). Membranes were washed in 10 mL of PBST for 5 minutes at room temperature with gentle shaking. The membranes were then incubated in 10 mL goat serum (5 %) for 1 hour at room temperature with gentle shaking. After blocking, the membranes were incubated with anti-m^{6}A antibody (1:1000) overnight at 4 °C with gentle shaking. Membranes were washed three times for 5 minutes each in 10 mL of PBST. Membranes were then incubated with goat anti-rabbit IgG-HRP (1:1000) for 1 hour at room temperature with gentle shaking. Membranes were developed after being washed four times for 10 minutes each in 10 mL of PBST. The total RNA was detected with methylene blue.

Quantitative analysis of m^{6}A—The levels of m^{6}A were quantified with EpiQuik™ m^{6}A RNA Methylation Quantification Kit and Epigenase m^{6}A Demethylase Activity/Inhibition

Assay Kit (Epigentek) according to the manufacturer's protocol. Briefly, 2 μL of negative control (NC), 2 μl of diluted positive control (PC), or 200 ng of sample RNA was added into the strip wells which pre-incubated with 80 μL binding solution. The strip plate was incubated at 37 °C for 1.5 hours. Washed strip was incubated with 50 μL of capture antibody at room temperature for 1 hour and incubated with 50 μL of detection antibody at room temperature for 0.5 hours. Washed Strip was incubated with 50 μL of enhancer solution at room temperature for 0.5 hours. 100 μL of developer solution was added to the washed strip and incubated at room temperature for 10 minutes away from light and 100 μL of stop solution was added for stopping reaction. Absorbance was measured on a microplate reader at 450 nm. The quantity of m^6A was calculated according to the following formula:

$$\text{m6A}\,\% = \frac{(\text{Sample OD} - \text{NC OD}) \div \text{S}}{(\text{PC OD} - \text{NC OD}) \div \text{p}} \times 100\,\%$$

Where S is the amount of input sample RNA in ng. P is the amount of input positive control (PC) in ng.

Quantitative analysis of m^6A RNA modification by LC-MS—Liquid Chromatography–Mass Spectrometry (LC-MS) assay was performed as previously described.[20] Briefly, mRNA was extracted with the magnetic mRNA isolation kit (NEB). The purified mRNA was digested with nucleoside digestion mix (M0649S, NEB). The N6-methyladenosine and adenosine were detected using Q Exactive Mass Spectrometers (Thermo Fisher).

LC-MS/MS analysis for drug concentration—Samples were analyzed with a LC-MS system which consisted of an Agilent (Palo Alto, CA, USA) 1200 SL autosampler and binary pump for sample introduction and chromatography, and an AB Sciex (Framingham, MA, USA) 4000Q mass spectrometer for sample detection and quantification. Each compound was quantified separately, employing a dilute and shoot method for extraction. For each assay, a gradient composed of acetonitrile and water with 0.1% formic acid was utilized. A Phenomenex (Torrance, CA, USA) Kinetex C18 column was used for the chromatography of both erlotinib and ALKBH5i, while a Phenomenex Asahipak column was used for the chromatography of GLCMi. The internal standards used were dasatinib (erlotinib), triapine (ALKBH5i) and methionine sulfoximine (GLCMi). The assays demonstrated linearity over the concentration range of 10-10,000 ng/mL for Erlotinib, 100-10,000 for ALKBH5i, and 20-10,000 for GLCMi, respectively. Linear regression with 1/y^2 weighting was applied for all three assays to ensure robustness and precision in the quantification process.

β-Galactosidase cell staining—Senescence was detected with β-Galactosidase Staining Kit (CST) according to the manufacturer's instructions. GSCs were cultured on a Matrigel-coated 6-well plate and inhibitors were administered. 1 ml of 1X Fixative Solution was added to each well after washing with PBS. The cells were fixed for 10-15 minutes at room temperature. Subsequently, the plate was rinsed twice with 1X PBS, then 1 ml of the β-Galactosidase Staining Solution was added to each well and the plate was incubated

at 37°C in a dry, non-CO2 incubator overnight. Finally, images were captured using a microscope.

ALT activity assay—ALT activity was detected with ALT activity assay kit (Sigma) according to the manufacturer's instructions. Serum samples were collected from mice with or without inhibitor administration. 100 μL of the reaction mix was added to each well of the assay plate. The contents were thoroughly mixed in each well by gentle pipetting. The assay plate was placed in an incubator set at 37°C. After 2–3 minutes of incubation, an initial measurement (Tinitial) was measured by the absorbance at 470 nm, then the incubation continued at 37°C and with absorbance measurements (A470) every 5 minutes until the value of the most active sample surpassed the absorbance value of the highest standard. The ALT activity was determined by the following equation:

$$ALT\ Activity = \frac{\mathrm{B} \times \text{sample Dilution Factor}}{(\mathrm{T}final - \mathrm{T}initial) \times V}$$

B = Amount (nmole) of pyruvate generated between $T_{initial}$ and T_{final}

V = sample volume (mL) added to well.

AST activity assay—AST activity was detected with AST activity assay kit (Sigma) according to the manufacturer's instructions. Serum samples were collected from mice with or without inhibitor administration. 100 μL of the reaction mix was added to each well of the assay plate. The contents were thoroughly mixed in each well by gentle pipetting, then the assay plate was placed in an incubator set at 37°C. After 2-3 minutes of incubation, an initial measurement (Tinitial) was measured at absorbance at 450 nm, then incubation continued at 37°C and with absorbance measurements (A450) every 5 minutes until the value of the most active sample surpassed the absorbance value of the highest standard. The AST activity was determined by the following equation:

$$AST\ Activity = \frac{\mathrm{B} \times \text{sample Dilution Factor}}{(\mathrm{T}final - \mathrm{T}initial) \times V}$$

B = Amount (nmole) of glutamate generated between T (initial) and T (final).

Reaction Time = $T_{final} - T_{initial}$ (minutes)

V = sample volume (mL) added to well

MeRIP-qPCR—The MeRIP was performed with the Magna MeRIP™ m^{6}A kit (17-1094, Millipore-Sigma) according to the manufacturer's instructions. Briefly, mRNA was fragmented by repeated heating at 94 °C for 5 minutes and vortexing. RNA was precipitated in ethanol, stored at −80 °C overnight, allowed to air dry, and resuspended in RNAase-free water. Magna ChIP Protein A/G Magnetic Beads were used for immunoprecipitation with 10 μg of the anti-m^{6}A antibody and 300 μg of total RNA for each reaction. Immunoprecipitation tubes were incubated for 2 hours at 4 °C. Beads were washed and RNA was eluted and purified using RNeasy mini kit. The RNA level was analyzed using

quantitative RT-PCR. The primers used in this study are listed as follows: GCLM 5'-ATGGGCACCGACAGCC-3' and 5'- TGCATGAGATACAGTGCATTCC-3'.

ROS Detection—The cellular ROS was detected with the ROS assay kit (ab 113851, Abcam) according to the manufacturer's instructions. Briefly, 1 * 105 cells were stained in culture media with 20 μM DCFDA for 30 minutes at 37°C. Then washing cells with 1X buffer after incubation. ROS level was analyzed on flow cytometer immediately after gently pipetting cells to single cell suspension.

QUANTIFICATION AND STATISTICAL ANALYSIS

All statistical analyses are described in the figure legends. For TCGA GBM vs. normal brain RNAseq analysis, four-way ANOVA controlling for sex, age, and ethnicity with the Benjamini and Hochberg false discovery rate (FDR) method was used for statistical analysis. For survival analyses, Cox proportional hazards and log-rank tests were used. For qPCR analyses, Student's t-test was used to assess statistical significance, when appropriate. Two-way repeated measures ANOVA was used for statistical analysis with Dunnett's multiple hypothesis test correction. For proliferation assays and limiting dilution assay, two-way repeated measures ANOVA was used for statistical analysis with Dunnett's multiple hypothesis test correction. The significance of differences was considered when the p-value was less than 0.05. The significance of differences was determined using GraphPad Prism 9 software. All data involving statistics are presented as mean ± SD or SEM.

Supplementary Material

Refer to Web version on PubMed Central for supplementary material.

ACKNOWLEDGMENTS

We appreciate the UCSD electron microscope core, and University of Pittsburgh mass spectrometry lab, and University of Pittsburgh biospecimen core for their work on electron microscope slides, and liquid chromatography-mass spectrometry assays, and histologic experiments respectively. This work was supported by NIH grants (CA197718, CA238662, CA268634, and NS103434 to J.N. Rich) and Defense Health Agency (HT9425-23-1-0689 to J. N. Rich). K. Yang was supported by the Computational Genomic Epidemiology of Cancer (CoGEC) Program at Case Comprehensive Cancer Center (T32CA094186), Young Investigator Award in Glioblastoma from ASCO Conquer Cancer Foundation, and RSNA Research Resident Grant.

INCLUSION AND DIVERSITY

We support inclusive, diverse, and equitable conduct of research.

REFERENCES

1. Ostrom QT, Price M, Neff C, Cioffi G, Waite KA, Kruchko C, and Barnholtz-Sloan JS (2022). CBTRUS Statistical Report: Primary Brain and Other Central Nervous System Tumors Diagnosed in the United States in 2015-2019. Neuro Oncol 24, v1–v95. 10.1093/neuonc/noac202. [PubMed: 36196752]
2. Stupp R, Hegi ME, Mason WP, van den Bent MJ, Taphoorn MJ, Janzer RC, Ludwin SK, Allgeier A, Fisher B, Belanger K, et al. (2009). Effects of radiotherapy with concomitant and adjuvant temozolomide versus radiotherapy alone on survival in glioblastoma in a randomised phase III study: 5-year analysis of the EORTC-NCIC trial. The Lancet. Oncology 10, 459–466. 10.1016/S1470-2045(09)70025-7. [PubMed: 19269895]

3. Verhaak RG, Hoadley KA, Purdom E, Wang V, Qi Y, Wilkerson MD, Miller CR, Ding L, Golub T, Mesirov JP, et al. (2010). Integrated genomic analysis identifies clinically relevant subtypes of glioblastoma characterized by abnormalities in PDGFRA, IDH1, EGFR, and NF1. Cancer Cell 17, 98–110. 10.1016/j.ccr.2009.12.020. [PubMed: 20129251]

4. Snuderl M, Fazlollahi L, Le LP, Nitta M, Zhelyazkova BH, Davidson CJ, Akhavanfard S, Cahill DP, Aldape KD, Betensky RA, et al. (2011). Mosaic amplification of multiple receptor tyrosine kinase genes in glioblastoma. Cancer Cell 20, 810–817. 10.1016/j.ccr.2011.11.005. [PubMed: 22137795]

5. Kim Y, Kim E, Wu Q, Guryanova O, Hitomi M, Lathia JD, Serwanski D, Sloan AE, Weil RJ, Lee J, et al. (2012). Platelet-derived growth factor receptors differentially inform intertumoral and intratumoral heterogeneity. Genes Dev 26, 1247–1262. 10.1101/gad.193565.112. [PubMed: 22661233]

6. Hamerlik P, Lathia JD, Rasmussen R, Wu Q, Bartkova J, Lee M, Moudry P, Bartek J Jr., Fischer W, Lukas J, et al. (2012). Autocrine VEGF-VEGFR2-Neuropilin-1 signaling promotes glioma stem-like cell viability and tumor growth. J Exp Med 209, 507–520. 10.1084/jem.20111424. [PubMed: 22393126]

7. Stommel JM, Kimmelman AC, Ying H, Nabioullin R, Ponugoti AH, Wiedemeyer R, Stegh AH, Bradner JE, Ligon KL, Brennan C, et al. (2007). Coactivation of receptor tyrosine kinases affects the response of tumor cells to targeted therapies. Science 318, 287–290. 10.1126/science.1142946. [PubMed: 17872411]

8. Dixit D, Prager BC, Gimple RC, Poh HX, Wang Y, Wu Q, Qiu Z, Kidwell RL, Kim LJY, Xie Q, et al. (2021). The RNA m6A Reader YTHDF2 Maintains Oncogene Expression and Is a Targetable Dependency in Glioblastoma Stem Cells. Cancer Discov 11, 480–499. 10.1158/2159-8290.CD-20-0331. [PubMed: 33023892]

9. Qiu Z, Zhao L, Shen JZ, Liang Z, Wu Q, Yang K, Min L, Gimple RC, Yang Q, Bhargava S, et al. (2022). Transcription Elongation Machinery Is a Druggable Dependency and Potentiates Immunotherapy in Glioblastoma Stem Cells. Cancer Discov 12, 502–521. 10.1158/2159-8290.CD-20-1848. [PubMed: 34615656]

10. Cui Q, Shi H, Ye P, Li L, Qu Q, Sun G, Sun G, Lu Z, Huang Y, Yang CG, et al. (2017). m(6)A RNA Methylation Regulates the Self-Renewal and Tumorigenesis of Glioblastoma Stem Cells. Cell Rep 18, 2622–2634. 10.1016/j.celrep.2017.02.059. [PubMed: 28297667]

11. Li F, Yi Y, Miao Y, Long W, Long T, Chen S, Cheng W, Zou C, Zheng Y, Wu X, et al. (2019). N(6)-Methyladenosine Modulates Nonsense-Mediated mRNA Decay in Human Glioblastoma. Cancer Res 79, 5785–5798. 10.1158/0008-5472.CAN-18-2868. [PubMed: 31530567]

12. Tassinari V, Cesarini V, Tomaselli S, Ianniello Z, Silvestris DA, Ginistrelli LC, Martini M, De Angelis B, De Luca G, Vitiani LR, et al. (2021). ADAR1 is a new target of METTL3 and plays a pro-oncogenic role in glioblastoma by an editing-independent mechanism. Genome Biol 22, 51. 10.1186/s13059-021-02271-9. [PubMed: 33509238]

13. Visvanathan A, Patil V, Arora A, Hegde AS, Arivazhagan A, Santosh V, and Somasundaram K (2018). Essential role of METTL3-mediated m(6)A modification in glioma stem-like cells maintenance and radioresistance. Oncogene 37, 522–533. 10.1038/onc.2017.351. [PubMed: 28991227]

14. Chai RC, Chang YZ, Chang X, Pang B, An SY, Zhang KN, Chang YH, Jiang T, and Wang YZ (2021). YTHDF2 facilitates UBXN1 mRNA decay by recognizing METTL3-mediated m(6)A modification to activate NF-kappaB and promote the malignant progression of glioma. J Hematol Oncol 14, 109. 10.1186/s13045-021-01124-z. [PubMed: 34246306]

15. Dong F, Qin X, Wang B, Li Q, Hu J, Cheng X, Guo D, Cheng F, Fang C, Tan Y, et al. (2021). ALKBH5 Facilitates Hypoxia-Induced Paraspeckle Assembly and IL8 Secretion to Generate an Immunosuppressive Tumor Microenvironment. Cancer Res 81, 5876–5888. 10.1158/0008-5472.CAN-21-1456. [PubMed: 34670781]

16. Visvanathan A, Patil V, Abdulla S, Hoheisel JD, and Somasundaram K (2019). N(6)-Methyladenosine Landscape of Glioma Stem-Like Cells: METTL3 Is Essential for the Expression of Actively Transcribed Genes and Sustenance of the Oncogenic Signaling. Genes (Basel) 10. 10.3390/genes10020141.

17. Yankova E, Blackaby W, Albertella M, Rak J, De Braekeleer E, Tsagkogeorga G, Pilka ES, Aspris D, Leggate D, Hendrick AG, et al. (2021). Small-molecule inhibition of METTL3

as a strategy against myeloid leukaemia. Nature 593, 597–601. 10.1038/s41586-021-03536-w. [PubMed: 33902106]

18. Su R, Dong L, Li C, Nachtergaele S, Wunderlich M, Qing Y, Deng X, Wang Y, Weng X, Hu C, et al. (2018). R-2HG Exhibits Anti-tumor Activity by Targeting FTO/m(6)A/MYC/CEBPA Signaling. Cell 172, 90–105 e123. 10.1016/j.cell.2017.11.031. [PubMed: 29249359]
19. Zhang S, Zhao BS, Zhou A, Lin K, Zheng S, Lu Z, Chen Y, Sulman EP, Xie K, Bogler O, et al. (2017). m(6)A Demethylase ALKBH5 Maintains Tumorigenicity of Glioblastoma Stem-like Cells by Sustaining FOXM1 Expression and Cell Proliferation Program. Cancer Cell 31, 591–606 e596. 10.1016/j.ccell.2017.02.013. [PubMed: 28344040]
20. Lv D, Gimple RC, Zhong C, Wu Q, Yang K, Prager BC, Godugu B, Qiu Z, Zhao L, Zhang G, et al. (2022). PDGF signaling inhibits mitophagy in glioblastoma stem cells through N(6)-methyladenosine. Developmental cell 57, 1466–1481 e1466. 10.1016/j.devcel.2022.05.007. [PubMed: 35659339]
21. Hassannia B, Vandenabeele P, and Vanden Berghe T (2019). Targeting Ferroptosis to Iron Out Cancer. Cancer Cell 35, 830–849. 10.1016/j.ccell.2019.04.002. [PubMed: 31105042]
22. Schonberg DL, Miller TE, Wu Q, Flavahan WA, Das NK, Hale JS, Hubert CG, Mack SC, Jarrar AM, Karl RT, et al. (2015). Preferential Iron Trafficking Characterizes Glioblastoma Stem-like Cells. Cancer Cell 28, 441–455. 10.1016/j.ccell.2015.09.002. [PubMed: 26461092]
23. Ravi VM, Will P, Kueckelhaus J, Sun N, Joseph K, Salie H, Vollmer L, Kuliesiute U, von Ehr J, Benotmane JK, et al. (2022). Spatially resolved multi-omics deciphers bidirectional tumor-host interdependence in glioblastoma. Cancer Cell 40, 639–655 e613. 10.1016/j.ccell.2022.05.009. [PubMed: 35700707]
24. Fang R, Chen X, Zhang S, Shi H, Ye Y, Shi H, Zou Z, Li P, Guo Q, Ma L, et al. (2021). EGFR/SRC/ERK-stabilized YTHDF2 promotes cholesterol dysregulation and invasive growth of glioblastoma. Nat Commun 12, 177. 10.1038/s41467-020-20379-7. [PubMed: 33420027]
25. Zhong L, Liao D, Zhang M, Zeng C, Li X, Zhang R, Ma H, and Kang T (2019). YTHDF2 suppresses cell proliferation and growth via destabilizing the EGFR mRNA in hepatocellular carcinoma. Cancer Lett 442, 252–261. 10.1016/j.canlet.2018.11.006. [PubMed: 30423408]
26. Bhat KPL, Balasubramaniyan V, Vaillant B, Ezhilarasan R, Hummelink K, Hollingsworth F, Wani K, Heathcock L, James JD, Goodman LD, et al. (2013). Mesenchymal differentiation mediated by NF-kappaB promotes radiation resistance in glioblastoma. Cancer Cell 24, 331–346. 10.1016/j.ccr.2013.08.001. [PubMed: 23993863]
27. Wei J, Liu F, Lu Z, Fei Q, Ai Y, He PC, Shi H, Cui X, Su R, Klungland A, et al. (2018). Differential m6A, m6Am, and m1A Demethylation Mediated by FTO in the Cell Nucleus and Cytoplasm. Mol Cell 71, 973–985.e975. 10.1016/j.molcel.2018.08.011. [PubMed: 30197295]
28. Wieduwilt MJ, and Moasser MM (2008). The epidermal growth factor receptor family: biology driving targeted therapeutics. Cell Mol Life Sci 65, 1566–1584. 10.1007/s00018-008-7440-8. [PubMed: 18259690]
29. Sun HL, Zhu AC, Gao Y, Terajima H, Fei Q, Liu S, Zhang L, Zhang Z, Harada BT, He YY, et al. (2020). Stabilization of ERK-Phosphorylated METTL3 by USP5 Increases m. Mol Cell 80, 633–647.e637. 10.1016/j.molcel.2020.10.026. [PubMed: 33217317]
30. Wang C, Xu H, Lin S, Deng W, Zhou J, Zhang Y, Shi Y, Peng D, and Xue Y (2020). GPS 5.0: An Update on the Prediction of Kinase-specific Phosphorylation Sites in Proteins. Genomics Proteomics Bioinformatics 18, 72–80. 10.1016/j.gpb.2020.01.001. [PubMed: 32200042]
31. Mack SC, Singh I, Wang X, Hirsch R, Wu Q, Villagomez R, Bernatchez JA, Zhu Z, Gimple RC, Kim LJY, et al. (2019). Chromatin landscapes reveal developmentally encoded transcriptional states that define human glioblastoma. J Exp Med 216, 1071–1090. 10.1084/jem.20190196. [PubMed: 30948495]
32. Miller TE, Liau BB, Wallace LC, Morton AR, Xie Q, Dixit D, Factor DC, Kim LJY, Morrow JJ, Wu Q, et al. (2017). Transcription elongation factors represent in vivo cancer dependencies in glioblastoma. Nature 547, 355–359. 10.1038/nature23000. [PubMed: 28678782]
33. Jiang L, Hao Y, Shao C, Wu Q, Prager BC, Gimple RC, Sulli G, Kim LJ, Zhang G, Qiu Z, et al. (2022). ADAR1-mediated RNA editing links ganglioside catabolism to glioblastoma stem cell maintenance. J Clin Invest 132. 10.1172/JCI143397.

34. Wang X, Lu Z, Gomez A, Hon GC, Yue Y, Han D, Fu Y, Parisien M, Dai Q, Jia G, et al. (2014). N6-methyladenosine-dependent regulation of messenger RNA stability. Nature 505, 117–120. 10.1038/nature12730. [PubMed: 24284625]
35. Wang Y, Li Y, Toth JI, Petroski MD, Zhang Z, and Zhao JC (2014). N6-methyladenosine modification destabilizes developmental regulators in embryonic stem cells. Nat Cell Biol 16, 191–198. 10.1038/ncb2902. [PubMed: 24394384]
36. Du H, Zhao Y, He J, Zhang Y, Xi H, Liu M, Ma J, and Wu L (2016). YTHDF2 destabilizes m(6)A-containing RNA through direct recruitment of the CCR4-NOT deadenylase complex. Nat Commun 7, 12626. 10.1038/ncomms12626. [PubMed: 27558897]
37. Park OH, Ha H, Lee Y, Boo SH, Kwon DH, Song HK, and Kim YK (2019). Endoribonucleolytic Cleavage of m(6)A-Containing RNAs by RNase P/MRP Complex. Mol Cell 74, 494–507 e498. 10.1016/j.molcel.2019.02.034. [PubMed: 30930054]
38. Zaccara S, and Jaffrey SR (2020). A Unified Model for the Function of YTHDF Proteins in Regulating m(6)A-Modified mRNA. Cell 181, 1582–1595 e1518. 10.1016/j.cell.2020.05.012. [PubMed: 32492408]
39. Pan X, Fang Y, Li X, Yang Y, and Shen HB (2020). RBPsuite: RNA-protein binding sites prediction suite based on deep learning. BMC Genomics 21, 884. 10.1186/s12864-020-07291-6. [PubMed: 33297946]
40. Jiang X, Stockwell BR, and Conrad M (2021). Ferroptosis: mechanisms, biology and role in disease. Nat Rev Mol Cell Biol 22, 266–282. 10.1038/s41580-020-00324-8. [PubMed: 33495651]
41. Fujihara KM, Zhang BZ, Jackson TD, Ogunkola MO, Nijagal B, Milne JV, Sallman DA, Ang CS, Nikolic I, Kearney CJ, et al. (2022). Eprenetapopt triggers ferroptosis, inhibits NFS1 cysteine desulfurase, and synergizes with serine and glycine dietary restriction. Sci Adv 8, eabm9427. 10.1126/sciadv.abm9427. [PubMed: 36103522]
42. Selberg S, Seli N, Kankuri E, and Karelson M (2021). Rational Design of Novel Anticancer Small-Molecule RNA m6A Demethylase ALKBH5 Inhibitors. ACS Omega 6, 13310–13320. 10.1021/acsomega.1c01289. [PubMed: 34056479]
43. Mitre AO, Florian AI, Buruiana A, Boer A, Moldovan I, Soritau O, Florian SI, and Susman S (2022). Ferroptosis Involvement in Glioblastoma Treatment. Medicina (Kaunas) 58. 10.3390/medicina58020319.
44. Bailey HH (1998). L-S,R-buthionine sulfoximine: historical development and clinical issues. Chem Biol Interact 111–112, 239–254. 10.1016/s0009-2797(97)00164-6.
45. Cilurzo F, Cristiano MC, Da Pian M, Cianflone E, Quintieri L, Paolino D, and Pasut G (2019). Overcoming Cancer Cell Drug Resistance by a Folic Acid Targeted Polymeric Conjugate of Buthionine Sulfoximine. Anticancer Agents Med Chem 19, 1513–1522. 10.2174/1871520619666190626114641. [PubMed: 31241440]
46. Liu M, Zhao Y, and Zhang X (2015). Knockdown of glutamate cysteine ligase catalytic subunit by siRNA causes the gold nanoparticles-induced cytotoxicity in lung cancer cells. PLoS One 10, e0118870. 10.1371/journal.pone.0118870. [PubMed: 25789740]
47. Nishizawa S, Araki H, Ishikawa Y, Kitazawa S, Hata A, Soga T, and Hara T (2018). Low tumor glutathione level as a sensitivity marker for glutamate-cysteine ligase inhibitors. Oncol Lett 15, 8735–8743. 10.3892/ol.2018.8447. [PubMed: 29928324]
48. Qin Y, Zhai Q, Li Y, Cao M, Xu Y, Zhao K, and Wang T (2018). Cyanidin-3-O-glucoside ameliorates diabetic nephropathy through regulation of glutathione pool. Biomed Pharmacother 103, 1223–1230. 10.1016/j.biopha.2018.04.137. [PubMed: 29864902]
49. Flaherty KT, Infante JR, Daud A, Gonzalez R, Kefford RF, Sosman J, Hamid O, Schuchter L, Cebon J, Ibrahim N, et al. (2012). Combined BRAF and MEK inhibition in melanoma with BRAF V600 mutations. N Engl J Med 367, 1694–1703. 10.1056/NEJMoa1210093. [PubMed: 23020132]
50. Eroglu Z, and Ribas A (2016). Combination therapy with BRAF and MEK inhibitors for melanoma: latest evidence and place in therapy. Ther Adv Med Oncol 8, 48–56. 10.1177/1758834015616934. [PubMed: 26753005]
51. Dossett LA, Kudchadkar RR, and Zager JS (2015). BRAF and MEK inhibition in melanoma. Expert Opin Drug Saf 14, 559–570. 10.1517/14740338.2015.1011618. [PubMed: 25648338]

52. Wei CM, Gershowitz A, and Moss B (1975). Methylated nucleotides block 5' terminus of HeLa cell messenger RNA. Cell 4, 379–386. 10.1016/0092-8674(75)90158-0. [PubMed: 164293]

53. Dubin DT, and Taylor RH (1975). The methylation state of poly A-containing messenger RNA from cultured hamster cells. Nucleic Acids Res 2, 1653–1668. 10.1093/nar/2.10.1653. [PubMed: 1187339]

54. Perry RP, Kelley DE, Friderici K, and Rottman F (1975). The methylated constituents of L cell messenger RNA: evidence for an unusual cluster at the 5' terminus. Cell 4, 387–394. 10.1016/0092-8674(75)90159-2. [PubMed: 1168101]

55. Carpenter G, and Cohen S (1990). Epidermal growth factor. The Journal of biological chemistry 265, 7709–7712. [PubMed: 2186024]

56. Huang PH, Xu AM, and White FM (2009). Oncogenic EGFR signaling networks in glioma. Science signaling 2, re6. 10.1126/scisignal.287re6. [PubMed: 19738203]

57. Uhm JH, Ballman KV, Wu W, Giannini C, Krauss JC, Buckner JC, James CD, Scheithauer BW, Behrens RJ, Flynn PJ, et al. (2011). Phase II evaluation of gefitinib in patients with newly diagnosed Grade 4 astrocytoma: Mayo/North Central Cancer Treatment Group Study N0074. Int J Radiat Oncol Biol Phys 80, 347–353. 10.1016/j.ijrobp.2010.01.070. [PubMed: 20510539]

58. Gao F, Wang Q, Zhang C, Zhang C, Qu T, Zhang J, Wei J, and Guo R (2021). RNA methyltransferase METTL3 induces intrinsic resistance to gefitinib by combining with MET to regulate PI3K/AKT pathway in lung adenocarcinoma. Journal of cellular and molecular medicine 25, 2418–2425. 10.1111/jcmm.16114. [PubMed: 33491264]

59. Wei J, Liu F, Lu Z, Fei Q, Ai Y, He PC, Shi H, Cui X, Su R, Klungland A, et al. (2018). Differential m(6)A, m(6)Am, and m(1)A Demethylation Mediated by FTO in the Cell Nucleus and Cytoplasm. Molecular cell 71, 973–985 e975. 10.1016/j.molcel.2018.08.011. [PubMed: 30197295]

60. Harris IS, Treloar AE, Inoue S, Sasaki M, Gorrini C, Lee KC, Yung KY, Brenner D, Knobbe-Thomsen CB, Cox MA, et al. (2015). Glutathione and thioredoxin antioxidant pathways synergize to drive cancer initiation and progression. Cancer cell 27, 211–222. 10.1016/j.ccell.2014.11.019. [PubMed: 25620030]

61. Vivian J, Rao AA, Nothaft FA, Ketchum C, Armstrong J, Novak A, Pfeil J, Narkizian J, Deran AD, Musselman-Brown A, et al. (2017). Toil enables reproducible, open source, big biomedical data analyses. Nat Biotechnol 35, 314–316. 10.1038/nbt.3772. [PubMed: 28398314]

62. Lv D, Li Y, Zhang W, Alvarez AA, Song L, Tang J, Gao WQ, Hu B, Cheng SY, and Feng H (2017). TRIM24 is an oncogenic transcriptional co-activator of STAT3 in glioblastoma. Nat Commun 8, 1454. 10.1038/s41467-017-01731-w. [PubMed: 29129908]

HIGHLIGHTS

- EGFR downregulates m^6A levels by promoting ALKBH5 nuclear localization
- SRC phosphorylates ALKBH5, reducing CRM1 mediated ALKBH5 nuclear export
- EGFR-ALKBH5 protects GCLM decay via m^6A to repress ferroptosis
- Pharmacologic ALKBH5 inhibitors augment efficacy of EGFR and GCLM inhibitors

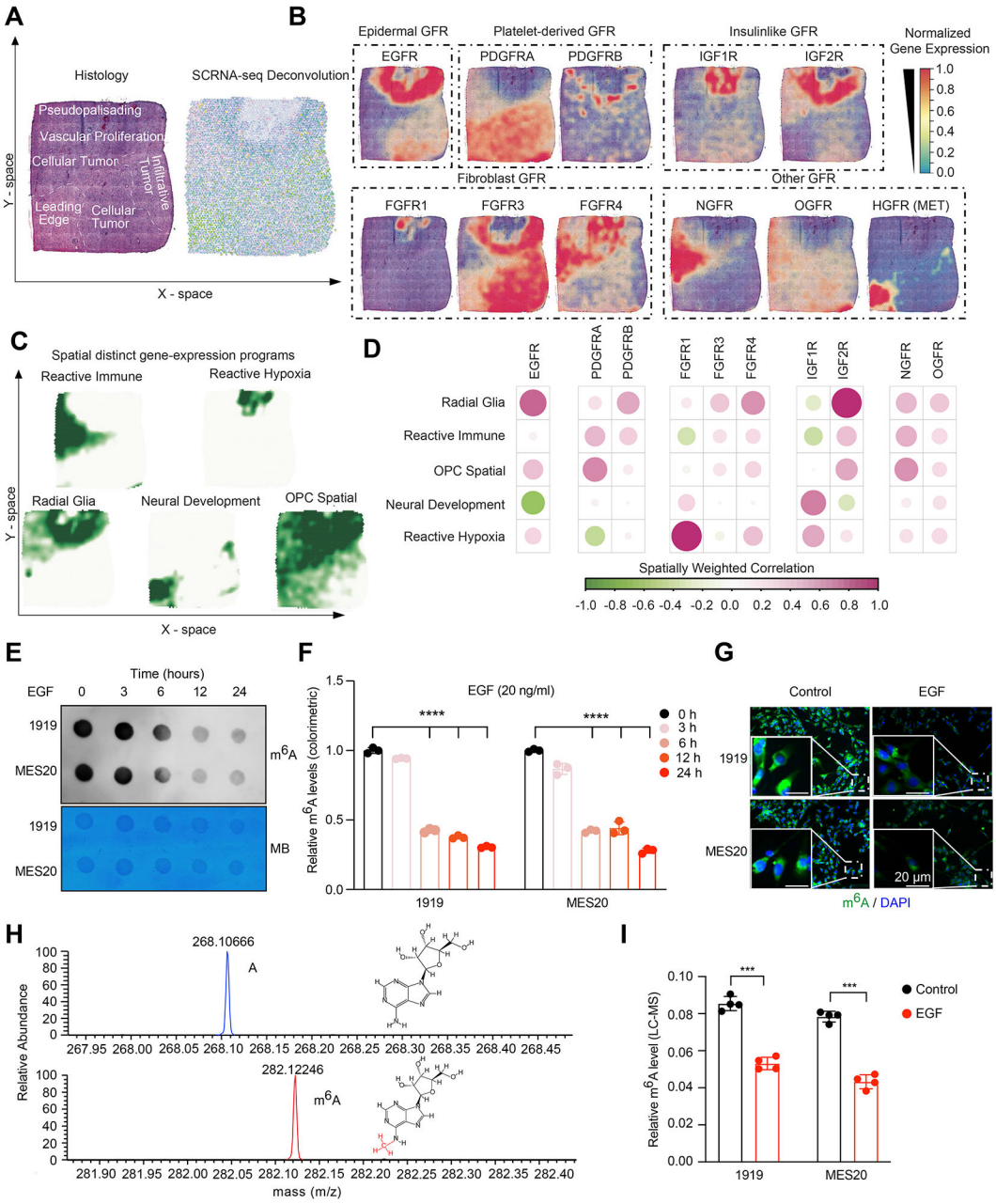

Figure 1. EGFR signaling regulates RNA m^{6}A levels in glioblastoma

(A) Spatial glioblastoma patient sample (UKF#275) with respect to histology (left) and cell type distribution using the latest reference dataset (~10^6 cells from 11 datasets) (right). Reference mapping was performed using SpaceXR and SPATA2 software. (B) Examples of spatial gene expression patterns of different GFRs. (C) Example of spatially resolved niches. (D) Spatially weighted correlation of niches and GFRs from 16 de novo glioblastomas. (E) EGF treatment decreases global m^{6}A levels in GSCs. Verification of the m^{6}A abundance in GSC RNA by dot blot (upper) and RNA level by methylene blue (below). (F) Colorimetric assay for global m^{6}A levels treated with or without EGF (two-tailed t-test, ***$p < 0.0001$, $n = 3$). (G) EGF treatment decreases global m^{6}A levels. Verification of the m^{6}A abundance

by immunofluorescent staining. (H) Representative LC-MS chromatogram and molecular structure of m^6A and A. (I) EGF treatment decreases global m^6A levels in GSCs RNA. Verification of m^6A abundance by LC-MS (two-tailed t-test, ***$p < 0.001$, $n = 4$).
See also Figure S1.

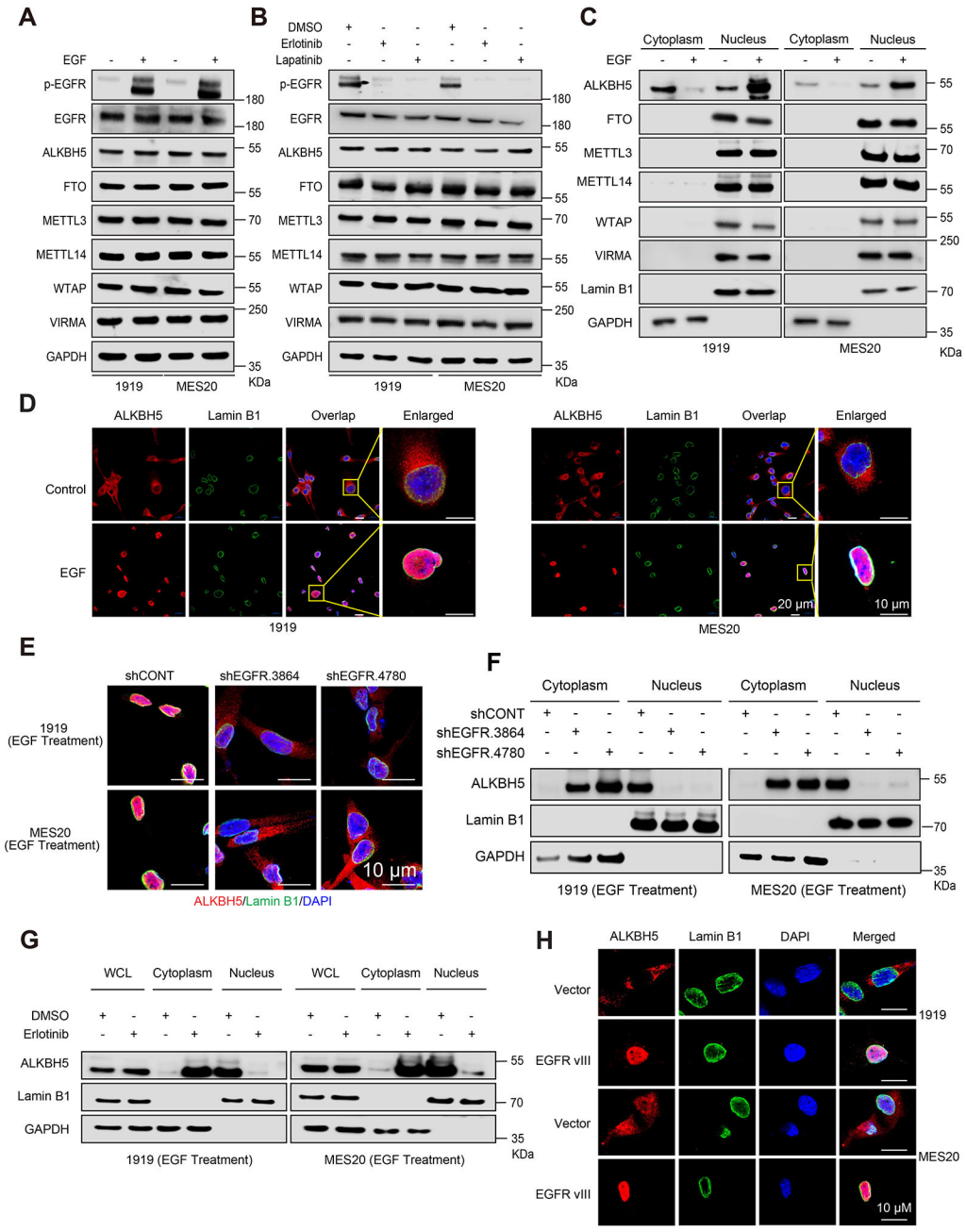

Figure 2. EGF-EGFR signaling regulates ALKBH5 nuclear localization

(A) Immunoblot of m^{6}A regulator protein levels in 1919 and MES20 cells after EGF treatment. (B) Immunoblot of m^{6}A regulators in GSCs with or without EGFR inhibitor treatment. (C) Immunoblot of m^{6}A regulator levels in subcellular fractions of GSCs with or without EGF treatment. (D, E) Subcellular localization of ALKBH5 in GSCs treatment with or without EGF (D) or upon EGFR knockdown (E) by immunofluorescence staining. (F) Immunoblot of ALKBH5 protein localization in GSCs with EGFR modulation. (G) Immunoblot of ALKBH5 protein localization in GSCs treated with or without erlotinib. (H)

Cellular localization of ALKBH5 in GSCs with or without EGFRvIII overexpression by immunofluorescence staining.
See also Figure S2.

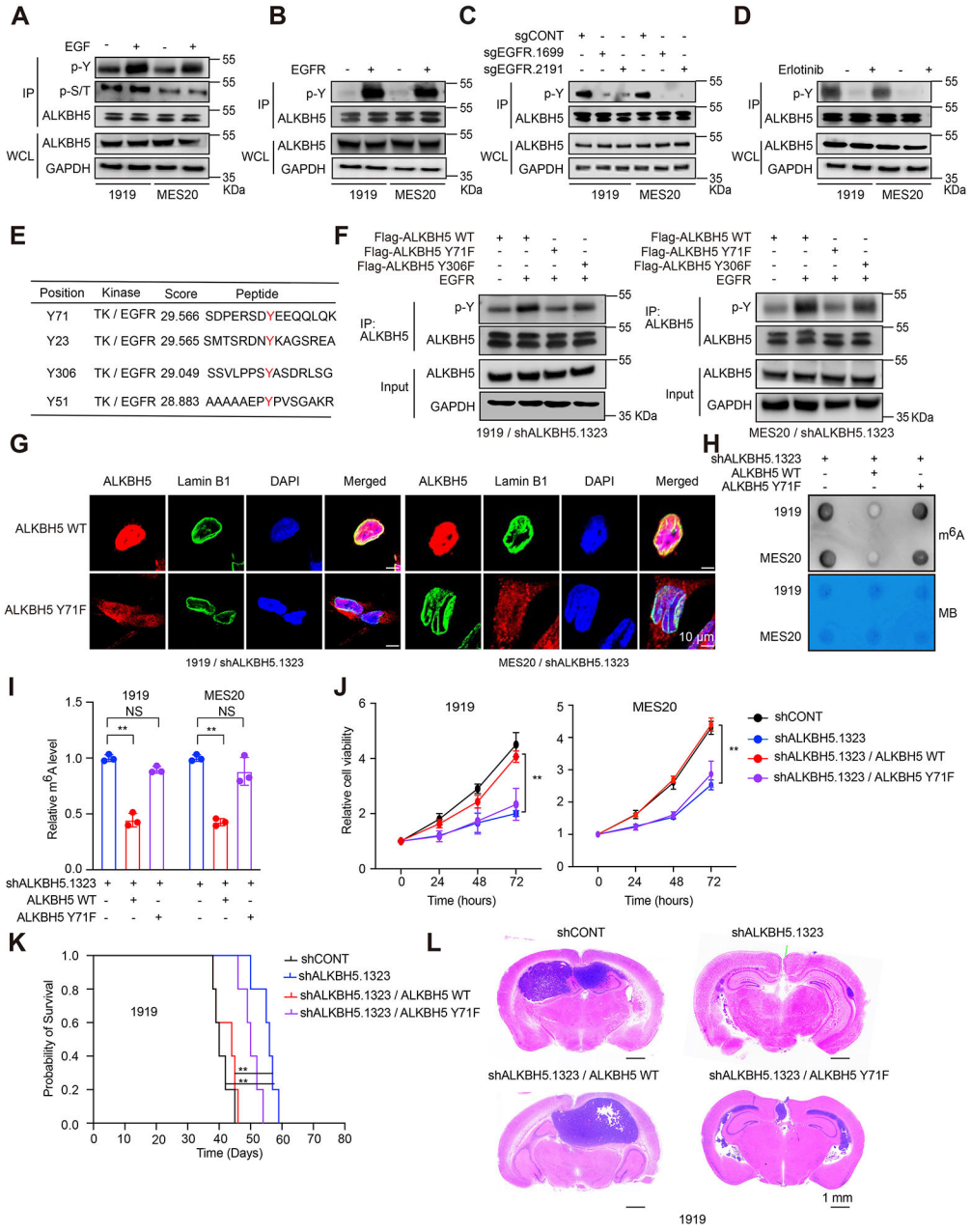

Figure 3. ALKBH5 Y71 phosphorylation is essential for its nuclear localization and functions in vitro and in vivo

(A-D) Immunoprecipitation of phosphorylated tyrosine in ALKBH5 from GSCs after EGF treatment (A), EGFR overexpression (B), EGFR knockout (C) and treatment with erlotinib (D). (E) EGFR-induced phosphorylated tyrosine residues in ALKBH5 protein. (F) Tyrosine phosphorylation in ALKBH5-depleted GSCs upon exogenous overexpression of ALKBH5 WT or Y71A or Y306A mutation, as determined by immunoprecipitation. (G) Cellular localization of ALKBH5 upon ALKBH5 knockdown in GSCs rescued with WT or mutated ALKBH5 by immunofluorescence staining. (H) ALKBH5 WT, but not the Y71F ALKBH5 mutant, decreases global m^{6}A levels in GSCs. Verification of the m^{6}A abundance by dot blot (upper) and RNA level by methylene blue (below). (I) Colorimetric assay for global

m^{6}A level in ALKBH5 knockdown GSCs upon ALKBH5 WT or mutation rescue (one-way ANOVA, **p < 0.01, n = 3). (J) Cell viability of GSCs upon ALKBH5 knockdown, either alone or in combination with ALKBH5 WT or Y71F overexpression. (one-way ANOVA, **p < 0.01, n = 3). (K) Survival curves of immunocompromised mice bearing intracranial xenografts driven from 1919 GSCs transduced with shALKBH5.1323 and ALKBH5 WT or Y71F overexpression. (Log-rank analysis, **p < 0.01). (L) Representative histology images of tumor-bearing brains. Brains were harvested after the presentation of the first neurological sign in any cohort.

See also Figure S3.

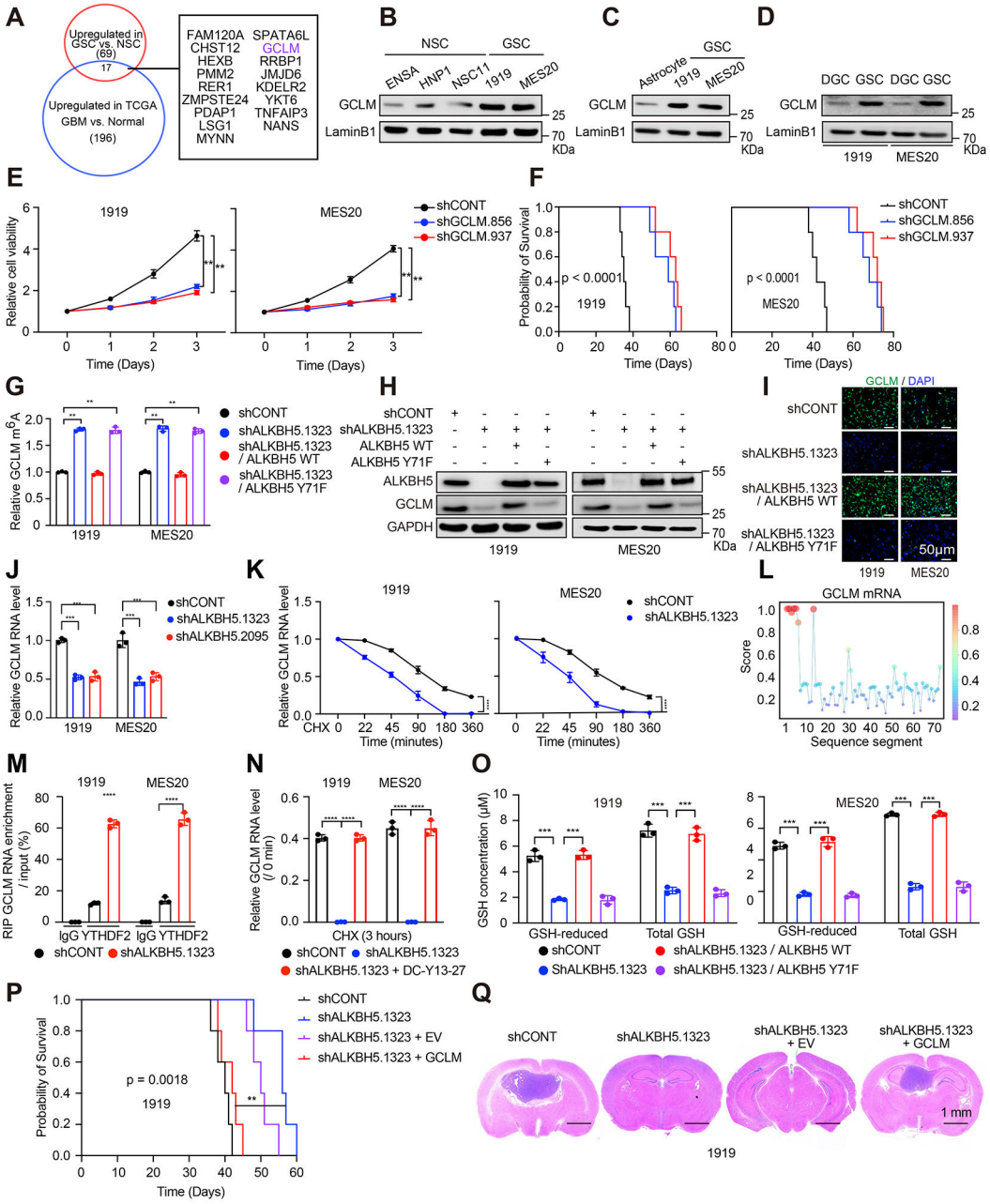

Figure 4. GCLM is a specific target of ALKBH5 in GSCs

(A) Overlap of ALKBH5 regulated genes that are highly expressed in GBM in general and GSCs specifically compared with normal brain or NSCs. (B-D) Immunoblotting detects GCLM expression in neural stem cells (B), astrocytes (C), and DGCs (D), and in GSCs. (E) Cell viability assay of GSCs transduced with shRNAs targeting GCLM (one-way ANOVA, **, $P < 0.01$, n = 3). (F) Survival curves show the time until the onset of neurological signs in intracranial xenografts derived from 1919 and MES20 transduced with two independent non-overlapping shRNAs (shGCLM.856 or shGCLM.937) targeting GCLM or a non-targeting shRNA (shCONT). (Log-rank analysis, *** $p < 0.001$,). (G) m^6A abundance on GCLM mRNA in 1919 and MES20 GSCs as quantified by MeRIP-qPCR

(one-way ANOVA **P < 0.01, n = 3). (H) Immunoblot of GCLM expression in ALKBH5 knockdown cell lines with ALKBH5 WT or Y71F mutation rescue. (I) GCLM expression in ALKBH5 knockdown GSCs with ALKBH5 WT or mutant Y71F expression, detected by immunofluorescence assay. (J) qPCR analysis of GCLM mRNA levels following ALKBH5. Student's t-test with Holm-Sidak multiple test correction. ***, p < 0.001. (K) ALKBH5 knockdown promotes GCLM mRNA decay in GSCs. qPCR analysis of mRNA level in GSCs treated with actinomycin D. (two-way ANOVA with Sidak multiple test correction, ***, p < 0.001). (L) The binding of YTHDF2 protein with GCLM RNA was predicted with RBPsuite. (M) RIP-qPCR assay for the enrichment of YTHDF2 in GCLM transcript in GSCs. (One-way ANOVA, ****, p < 0.0001). (N) qPCR analysis of GCLM mRNA level following knockdown with shALKBH5.1323 and treatment with or without YTHDF2 inhibitor (DC-Y13-27). Two-way ANOVA with Sidak multiple test correction. ****, p < 0.0001. (O) Reduced and total GSH concentration in ALKBH5 knockdown GSCs with ALKBH5 WT or mutant Y71F expression (one-way ANOVA, ***P < 0.001, n = 3). (P) Survival curves of immunocompromised mice bearing intracranial xenografts driven from 1919, transduced with shALKBH5.1323 with or without GCLM overexpression. (Log-rank analysis, **, p < 0.01) (Q) Representative histology images of sections of tumor-bearing brains. Tumors were derived from 1919 cells transduced with or without GCLM knockdown. Brains were harvested after the presentation of first neurological sign in any cohort.

See also Figure S4.

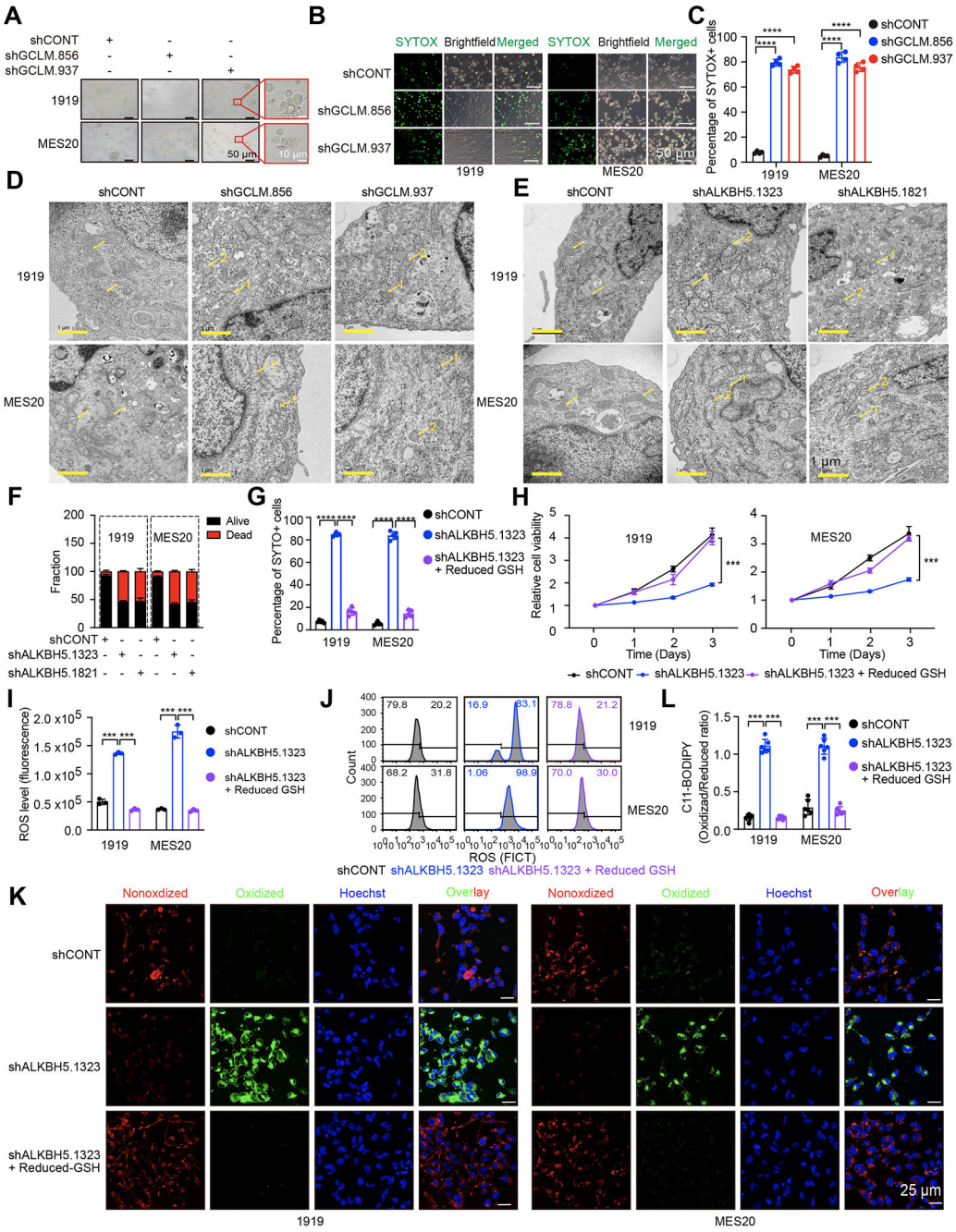

Figure 5. ALKBH5 inhibits ferroptosis via GCLM

(A) Morphological assay of ferroptosis in GSCs upon GCLM knockdown. (B) SYTOX staining to detect cell death in GSCs. (C) Quantification of SYTOX positive cells from panel B (one-way ANOVA, ****p < 0.0001, n = 4). (D) Electron microscopy detects mitochondrial morphology in GSC 1919 targeting GCLM. (E) Electron microscopy detects mitochondrial morphology in GSC 1919 targeting ALKBH5. (F) Cell death assay of GSCs transduced with shRNAs targeting ALKBH5 or a shCONT. (G) SYTOX staining to detect cell death in ALKBH5 knockdown GSCs treated with or without reduced GSH (one-way ANOVA, ****p < 0.0001, n = 5). (H) Cell viability assay of ALKBH5 depleted GSCs,

treated with or without reduced GSH (one-way ANOVA, ***$p < 0.001$, $n = 3$). (I, J) ROS assay of ALKBH5 knockdown GSCs, treated with or without reduced GSH by fluorescence microplate assay (I) and flow cytometry measurement (J) (one-way ANOVA, ***$p < 0.001$, $n = 3$). (K) Lipid ROS detection using C11 BODIPY 581/591 (C11) in GSCs. (L) Quantification of the levels of lipid ROS in panel K (one-way ANOVA, ***$p < 0.001$, $n = 6$).

See also Figure S5.

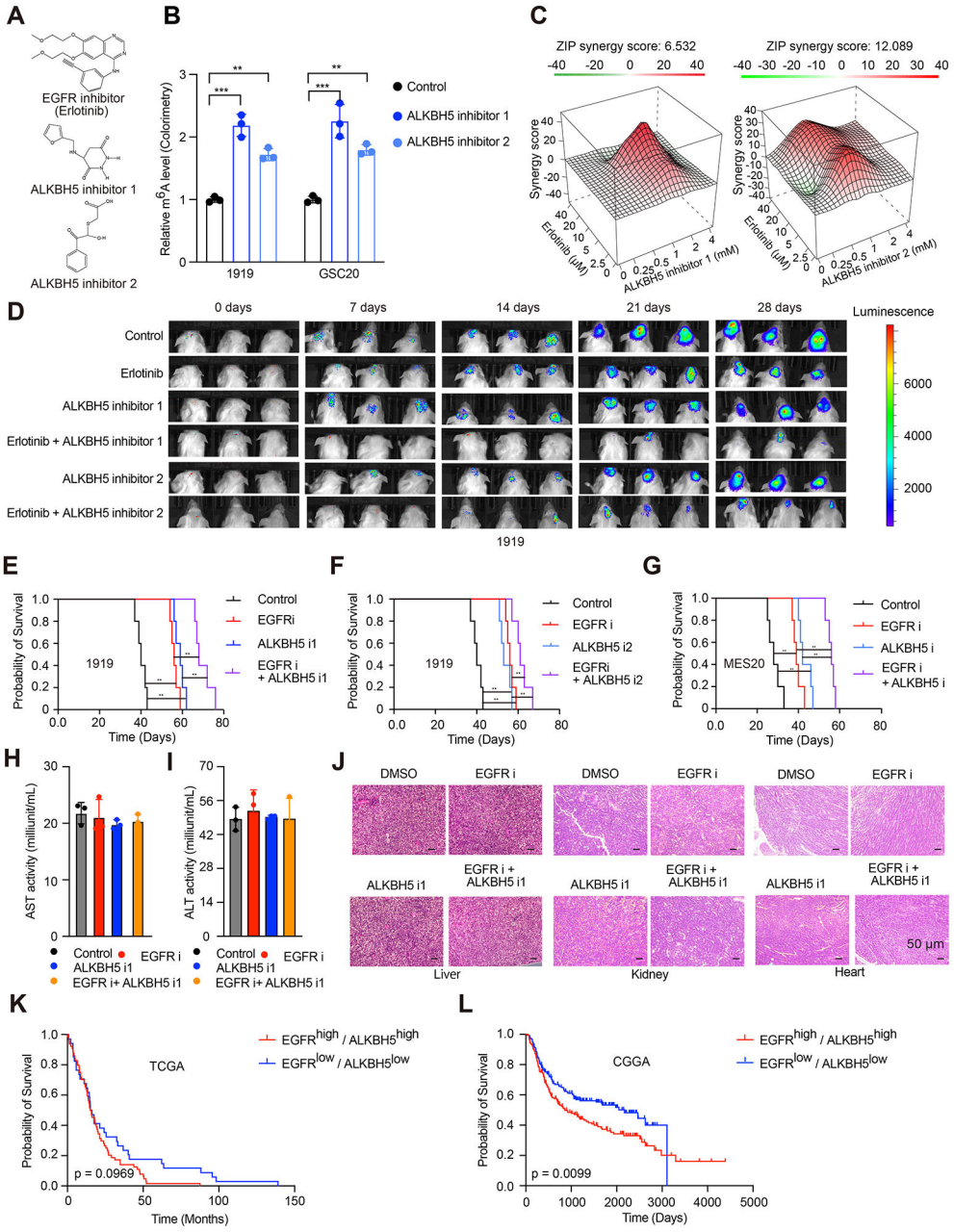

Figure 6. Pharmacologic targeting of ALKBH5 augments anti-tumor efficacy of EGFR

(A) Structures of ALKBH5i1, ALKBH5i2, and erlotinib. (B) Role of ALKBH5i on global m^6A levels in GSCs. Verification of the m^6A abundance by Colorimetric assay (two-tailed t-test, ***$p < 0.001$, **$p < 0.01$, $n = 3$). (C) Calculation and visualization of synergy scores for drug combinations of ALKBH5i and erlotinib. (D) In vivo bioluminescent imaging of tumors from respective experimental groups. (E) Survival curves of tumor-bearing mice from orthotopic intracranial xenograft implantation of 1919, treated with PBS, ALKBH5i1 (50 mg/kg), Erlotinib (20 mg/kg), or their combined treatment. (Log-rank test, **$p < 0.01$) (F) Survival curves of tumor-bearing mice from orthotopic intracranial xenograft derived from 1919 GSCs, treated with PBS, ALKBH5i2 (25 mg/kg), and erlotnib (20 mg/kg) or

their combined treatment. (Log-rank test, **p < 0.01). (G) Survival curves of tumor-bearing mice from orthotopic intracranial xenograft implantation of MES20, treated with PBS, ALKBH5i1 (50 mg/kg), EGFR inhibitor (50 mg/kg), or their combined treatment. (Log-rank test, **p < 0.01) (H-I) AST activity (H) and ALT (I) in mice with erlotinib (50 mg/ kg) or ALKBH5i1 treatment (50 mg/kg). (J) Histological analysis of liver, lung, and kidney of mice with erlotinib (50 mg/kg) or ALKBH5i1 (50 mg/kg) treatment. (K, L) Survival analysis of patient cohorts stratified into high vs. low expression levels of EGFR, ALKBH5 transcriptional score with the median as the cutoff in TCGA (K) and CGGA (L) GBM-LGG RNA-seqV2 dataset. P-values were calculated with log-rank test.
See also Figure S6.

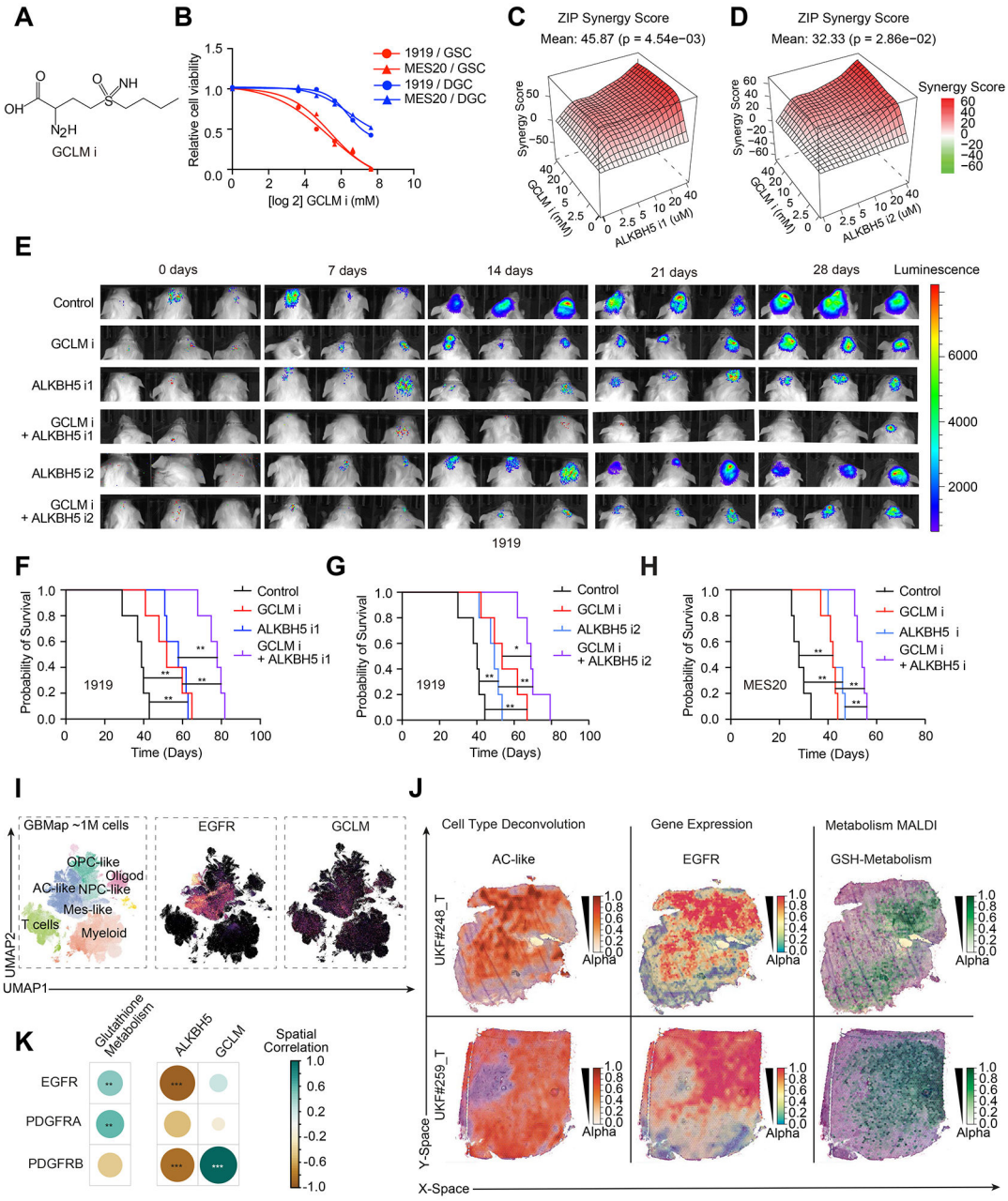

Figure 7. Targeting GCLM induces ferroptosis and generates an anti-tumor efficacy in GSCs

(A) Molecular structure of BSO. (B) Viability assay of paired GSCs and DGCs treated with the GCLM inhibitor. (C, D) Synergy score of GSC 1919 treated with ALKBH5i1 (C) or ALKBH5i2 (D) and BSO. (E) Luciferase image of tumors from respective experimental groups. (F) Survival curves of tumor-bearing mice from orthotopic intracranial xenograft implantation of 1919, treated with ALKBH5i1 (25 mg/kg), BSO (50 mg/kg), or their combined treatment. (Log-rank test, **p < 0.01) (G) Survival curves of tumor-bearing mice from orthotopic intracranial xenograft implantation of 1919, treated with ALKBH5i2 (25 mg/kg), BSO (50 mg/kg), or their combined treatment. (Log-rank test, **, p < 0.01). (H) Survival curves of tumor-bearing mice from orthotopic intracranial xenograft implantation

of MES20, treated ALKBH5i1 (50 mg/kg), BSO (50 mg/kg), or their combined treatment. (Log-rank test, **p < 0.01) (I) Expression of EGFR and GCLM at single cell level. (J, K) Spatially weighted correlation analysis of EGFR and GSH metabolism in glioblastoma specimens (one-way ANOVA, **p < 0.01, ***p < 0.001, n = 16).
See also Figure S7.

KEYRESOURCESTABLE

REAGENT or RESOURCE	SOURCE	IDENTIFIER
Antibodies		
PhosphoPlus® EGFR (Tyr1068) Antibody	Cell Signaling Technology	Cat# 3777, RRID:AB_2096270
EGF Receptor (D38B1) XP Rabbit mAb	Cell Signaling Technology	Cat# 4267; RRID:AB_2246311
EGFR Monoclonal Antibody (H11)	Thermo Fisher Scientific	Cat# MA5-13070, RRID:AB_10977527
Anti-ALKBH5 Antibody	Millipore	Cat# ABE547; RRID: RRID:AB_2687970
METTL3 Polyclonal antibody	Proteintech	Cat#15073-1-AP; RRID:AB_2142033
METTL14 Polyclonal antibody	Proteintech	Cat#26158-1-AP; RRID:AB_2800447
FTO Polyclonal antibody	Proteintech	Cat#27226-1-AP; RRID:AB_2880809
WTAP Monoclonal antibody	Proteintech	Cat# 60188-1-Ig; RRID:AB_10859484
VIRMA/KIAA1429 Polyclonal antibody	Proteintech	Cat# 25712-1-AP; RRID:AB_2880204
Recombinant Anti-FTO antibody	Abcam	Cat# ab126605, RRID:AB_11127120
Methyltransferase like 3 Antibody	Novus Bio	Cat# NBP3-03290
CRM1 antibody	Proteintech	Cat# 27917-1-AP, RRID:AB_2881009
KPNA2 antibody	Proteintech	Cat# 10819-1-AP, RRID:AB_2265526
Importin Beta 1 antibody	Proteintech	Cat# 10077-1-AP, RRID:AB_2133977
GCLM antibody	Proteintech	Cat# 14241-1-AP, RRID:AB_210783
HER2/ErbB2 Polyclonal antibody	Proteintech	Cat#18299-1-AP RRID:AB_2099264
ErbB3 Monoclonal Antibody	ThermoFisher	Cat# MA1-860 RRID:AB_325378
ERBB4 Polyclonal antibody	Proteintech	Cat# 19943-1-AP RRID:AB_10646486
EGFRvIII	ThermoFisher	Cat#MA5-36216 RRID:AB_2884050
YTHDF2	Proteintech	Cat#24744-1-AP RRID:AB_2687435
GAPDH	Proteintech	Cat# HRP-60004; RRID:AB_2737588
m^6A Antibody	Sigma	Cat# ABE572-I-100UG; RRID:AB_2892214
HRP-linked anti-Rabbit lgG	Cell Signaling Technology	Cat# 7074S; RRID:AB_2099233
HRP-linked anti-Mouse lgG	Cell Signaling Technology	Cat# 7076S; RRID:AB_209923
Goat anti-Rabbit IgG, Fluor 488	ThermoFisher	Cat# A32731TR; RRID:AB_2866491
Goat anti-Mouse lgG, Fluor 568	ThermoFisher	Cat# A-11031; RRID: AB_144696
Chemicals, Peptides and Recombinant Proteins		
Recombinant Human EGF	R&D Systems	Cat# 236-EG-01M
Recombinant Human FGF	R&D Systems	Cat# 4114-TC-01M
B27 supplement	ThermoFisher	Cat# 17504044
Neurobasal media	ThermoFisher	Cat# 12348017
Sodium pyruvate	ThermoFisher	Cat# 11360070
GlutaMAX	ThermoFisher	Cat# 35050061
Penicillin-Streptomycin	Thermofisher	Cat# 15140122
O.C.T compound	Saakura	Cat#4583
Erlotinib	MedChem Express	Cat# HY-50896
Lapatinib	Cayman	Cat# 11493
Buthionine sulfoximine	Cayman	Cat# 14484
ALKBH5 inhibitor 1	Molport	MolPort-002-122-434

REAGENT or RESOURCE	SOURCE	IDENTIFIER
ALKBH5 inhibitor 2	Enamine Ltd	EN300-14040
RSL3	MedChem Express	HY-100218A
Erastin	Cayman	17754
Sorafenib	MedChem Express	HY10201
SRC inhibitor 1	MedChem Express	HY-101053
Selinexor	Selleck Chem	S7252
Liproxstatin-1	Cayman	17730
FIN56	MedChem Express	HY-103087
Liproxstatin-1	Cayman	17730
DC-Y13-27	MedChem Express	HY-154919
DAPI	Sigma	Cat# 10236276001
Hoechst 33342	ThermoFisher	Cat# H3570
LipoD293	SignaGen Laboratories	Cat# SL100668
Lenti-X concentrator	Takara	Cat# 631232
Polybrene	Sigma	Cat# TR-1003
Critical commercial assays		
CellTiterGlo	Promega	Cat# G7571
EpiQuik™ m^{6}A RNA Methylation Quantification Kit	Epigentek	Cat# P-9005-96
Epigenase m^{6}A Demethylase Activity/Inhibition Assay Kit (Colorimetric)	Epigentek	Cat# P-9013-48
Chromatin Immunoprecipitation Kit	Sigma	Cat# 17-295
Direct-zol RNA kits	ZYMO research	Cat# R2061
Magnetic mRNA Isolation Kit	NEB	Cat# S1550S
Magna MeRIP™ m^{6}A Kit	Millipore-sigma	Cat# 17-1094
Q5® Site-Directed Mutagenesis Kit	NEB	Cat# E0554S
Site-Directed Mutagenesis Kit	Agilent	Cat# 200523
DCFDA / H2DCFDA - Cellular ROS Assay Kit	Abcam	Cat# ab113851
Cell Fractionation Kit	CST	Cat# 9038
Lipid Peroxidation Kit	ThermoFisher	Cat# C10445
SYBR™ Green Master Mix	ThermoFisher	Cat# A25742
PrimeScript™ RT Master Mix	Takara	Cat# RR036A
GeneJET Plasmid Miniprep Kit	ThermoFisher	Cat# K0502
PureLink™ HiPure Plasmid Midiprep Kit	ThermoFisher	Cat# K210005
Nucleoside Digestion Mix	NEB	Cat# M0649S
Senescence β-Galactosidase Staining Kit	CST	Cat#9860
SDS-PAGE	Invitrogen	Cat# NP0323BOX
Deposited data		
Raw m6A-sequencing data	Gene Expression Omnibus	GSE158742
Raw GSC RNA-sequencing data	Gene Expression Omnibus	GSE119834
Experimental models: Cell lines		
Cell line	1919	Patient derived
Cell line	MES20	Patient derived

REAGENT or RESOURCE	SOURCE	IDENTIFIER
Cell line	Human Astrocyte	ScienCell, Cat# 1850
Cell line	NSC11	Alstem, Cat# hNSC11
Cell line	ENSA	Millipore Sigma, Cat# SCC003
Cell line	HEK293T	ATCC, Cat# CRL-11268
competent cell	DH5α	ThermoFisher, Cat# 18265017
Experimental models: organisms/strains		
NSG Mice	The Jackson Laboratory	NOD.Cg-Prkdcscid Il2rgtm1Wjl/SzJ
Recombinant DNA		
EGFR WT	Addgene	Cat# 11011
PLVX-PURO-ALKBH5 WT	Clonetech	ALKBH5 WT
PLVX-PURO-ALKBH5 Y71F	Clonetech	ALKBH5 Y71F
PLVX-PURO-ALKBH5 Y306F	Clonetech	ALKBH5 Y306F
PLX304-GCLM	DNASU Plasmid	HsCD00435701
shEGFR.3864	Sigma	Cat# TRCN0000121068
shEGFR.4780	Sigma	Cat# TRCN0000010329
shALKBH5.1821	Sigma	Cat# TRCN0000064783
shALKBH5.1788	Sigma	Cat# TRCN0000064786
shSRC.662	Sigma	Cat# TRCN0000038150
shSRC.1593	Sigma	Cat# TRCN0000038149
shGCLM.856	Sigma	Cat# TRCN0000290874
shGCLM.937	Sigma	Cat# TRCN0000290800
Software and algorithms		
Endnote X9	https://endnote.com	Clarivate
GraphPad Prism v6.01	https://www.graphpad.com	GraphPad Prism
Adobe illustrator	https://www.adobe.com	Adobe
Image J	https://imagej.nih.gov/ij	National Institutes of Health
FLOWJO	https://www.flowjo.com	BD
CGGA	http://cgga.org.cn	CGGA
TCGA	https://portal.gdc.cancer.gov/	NIH
JASPAR	http://jaspar.genereg.net	JASPAR
GPS 5.0	http://gps.biocuckoo.cn/online.php	GPS
SpaceXR	https://github.com/dmcable/spacexr	SpaceXR
SPATA2	https://themilolab.github.io/SPATA2/	SPATA2
WGCNA	https://cran.r-project.org/web/packages/WGCNA/index.html	WGCNA